REVIEW

Open Access

Nonlinear plasmonics: second-harmonic generation and multiphoton photoluminescence

Jiyong Wang[1*] , Lei Zhang[2,3] and Min Qiu[2,3*]

*Correspondence:
jiyongwang@hdu.edu.cn;
qiumin@westlake.edu.cn

[1] Ministry of Education
Engineering Research Center
of Smart Microsensors
and Microsystems, School
of Electronics and Information,
Hangzhou Dianzi University,
Hangzhou 310018, China
[2] Key Laboratory of 3D
Micro/Nano Fabrication
and Characterization
of Zhejiang Province, School
of Engineering, Westlake
University, 18 Shilongshan Road,
Hangzhou 310024, Zhejiang
Province, China
[3] Institute of Advanced
Technology, Westlake
Institute for Advanced
Study, 18 Shilongshan Road,
Hangzhou 310024, Zhejiang
Province, China

Abstract

The study on the nonlinear optical responses arising from plasmonic nanoantennas, known as nonlinear plasmonics, has been massively investigated in recent years. Among the most basic nonlinear optical responses, second-harmonic generation (SHG) and multiphoton photoluminescence (MPL), two-photon photoluminescence in particular, has aroused extensive interests, due to their distinct properties of being ultrasensitive to the spatial symmetry and ultrafast response time of hot electrons. In this review, we give insights into fundamental roles dominating the radiations of such nonlinear optical processes and their recent research advances. Different from other reviews on nonlinear plasmonics, which mainly focused on parametric processes, this review pays equal attentions to the incoherent process of MPL. An in-depth description on the excitation and emission processes of MPL in accordance with recent studies is fully presented. By using the high 'symmetry rule' of SHG and ultrafast response time of MPL, advanced applications in surface enhanced spectroscopy, ultra-sensitive photodetector, biosensor and ultrafast laser pulses are highlighted in the end.

Introduction

Nonlinear optical phenomena have an indication that the response of a material system to an applied optical field depends nonlinearly on the strength of the optical field [1]. The optical responses induced by the light-mater interactions can be characterized by the polarization P. When the excitation electric field becomes intensive, especially in the focus volume of ultrafast laser pulses, the polarization induced involves not only linear responses P_L, but also nonlinear parts P_{NL}. This can be represented mathematically as [1]: $P(\omega) = \varepsilon_0 \chi^{(1)} E(\omega) + \varepsilon_0 (\chi^{(2)} E(\omega)^2 + \chi^{(3)} E(\omega)^3 + ...)$, where ε_0 is the permittivity of free space, $\chi^{(1)}$, $\chi^{(2)}$ and $\chi^{(3)}$ are the first three terms of susceptibilities, which are described as a second, third, fourth, ... rank of tensor in practice. $\chi^{(1)}$ leads to the linear optical responses and higher orders of susceptibilities lead to the study of nonlinear optics [1]. Nonlinear optics was established shortly after the development of the first laser system in the world [2, 3]. The related optical processes involving optical Kerr effect [4], optical phase conjugation [5, 6], four-wave mixing [7, 8], Raman amplification [9–11], stimulated Brillouin scattering [12, 13], multi-photon absorption [14, 15] and multiple

photoionization [16–18] were systemically investigated in the last several decades [19]. Their advanced applications range from optical fiber [20], optical switch [21, 22], photonic crystal [23, 24], super continuum light source [25, 26] and other optical devices to the modern plasmonic nanostructures [19].

Plasmons are generated by the coherent oscillations of conduction-electrons in response to incident light. When the light interacts with nanoparticles (NPs) whose sizes are smaller than the excitation wavelength, a local charge oscillation around NP is produced in resonance with the light frequency, which is well known as localized surface plasmon resonance (LSPR) [27, 28]. This capability of restricting the light at a nanoscale dimension provides NPs with tremendous unique features, including large electromagnetic field enhancements [29–31], high photothermal conversion efficiency [32–34], and rich spectral responses [15, 35–37].

Compared to linear optical processes, such as scattering [38–40], absorption [38, 41, 42] and one-photon photoluminescence (OPL) emission [35, 43], the generation of nonlinear optical signals requires a much stronger excitation field. Plasmonic nanoantennas can be used for the excitation of these optical processes since the field intensity is hugely enhanced by some orders of magnitude in their vicinities thanks to the LSPRs [15]. Their influences on nonlinear optical properties of plasmonic nanoantennas such as SHG [19, 44–53], two-photon photoluminescence (TPL) [36, 37], third and higher harmonics generation (THG and HHG) [54–56], four-wave mixing [57] as well as multi-photon photoluminescence (MPL) [14, 58, 59] have been thoroughly investigated. The potential applications are explored as well, ranging widely from nonlinear plasmonic sensing [60, 61], ultrasensitive photodetector [62], ultrafast laser pulse generation [63, 64] and so on. Nonlinear plasmonics, as a branch of nano optics, which merges the knowledge from both nonlinear optics and plasmonics, has emerged recently [3, 19].

Among different nonlinear optical processes from plasmonic nanoantennas, SHG and TPL are among the most basic second-order and third-order of nonlinear optical responses, and earn particular interests in single NP detection [65, 66], laser beam characterization [67, 68], symmetry imaging [6, 60, 69], fluorescence microscopy and spectroscopy [70, 71]. In this review, physical insights into fundamental rules of SHG and MPL radiation and their advanced applications are systemically discussed. Being alternative to recent reviews on nonlinear plasmonics [3, 72, 73], which mainly focused on the coherent nonlinear processes such as SHG, THG and FWM, this review pays sufficient attentions to the incoherent process of MPL. An in-depth description on excitation and emission process of MPL in accordance with the studies in recent years is fully presented. By using the high 'symmetry rule' from SHG and ultrafast response time of hot electrons from MPL, advanced applications in surface enhanced spectroscopy, ultrasensitive photodetector, biosensor and ultrafast laser pulses are highlighted in the end of the review.

This review is organized as follows. In session 2, two dominant factors including resonance effects and mode matching which lead to a strong far-field SHG are selected and analyzed. We emphasize the first contribution, which is then further divided into two cases: resonance effect in the fundamental and SH fields. In session 3, the physical mechanisms of three stages of MPL are discussed sequentially: absorption, relaxation and emission. In the absorption process, two mechanisms are compared and analyzed:

coherent two-photon absorption and two sequential one-photon absorption. In the relaxation process, we focus on the electrons thermalization dynamics and thermal damaging threshold, which are both tough topics rare studies in nonlinear plasmonic touch. In the emission process, two emission channels involving carriers recombination and plasmon emission will be introduced and explained in details. New promising applications of SHG and MPL that could be utilized in practice are reviewed in the session 4. The conclusions and outlooks are given in the end.

SHG

Among different nonlinear optical processes, SHG has advantages of being sensitive to the centrosymmetry of plasmonic nanostructures as well as their spatial configurations [19, 66, 74–77]. SHG is a coherent scattering process in terms of the second order of susceptibility. From the quantum view, SHG can be regarded as "absorbing" two photons with the frequency ω from a lower energy level to a virtual energy level followed by the generation of one photon with doubled frequency 2ω [78], as shown in Fig. 1a. It is known that SHG is forbidden in the bulk of centro-symmetric media within dipolar approximation [79]. Nevertheless, this symmetry is broken at the boundary between two centro-symmetric medias, and SHG can arise from the surfaces of metallic nanostructure [3, 80–82]. In 1968, Bloembergen et. al. attributed the generation of SHG arising from centrosymmetric materials to bulk contributions induced by electric quadrupoles and magnetic dipoles, as well as surface contributions from the dipoles at interfaces where the symmetry breaks [83]. The surface SHG becomes more and more predominant as the surface-to-volume ratio increases. With respect to NPs, the bulk SHG can be neglected due to the high surface-to-volume ratio [3, 15].

Classically, the fundamental near-field driven by incoming wave induces a nonlinear surface polarization due to the nonlinear surface susceptibility χ_{surf}. χ_{surf} is described using a third rank tensor including 27 elements, as it is shown in Fig. 1b.
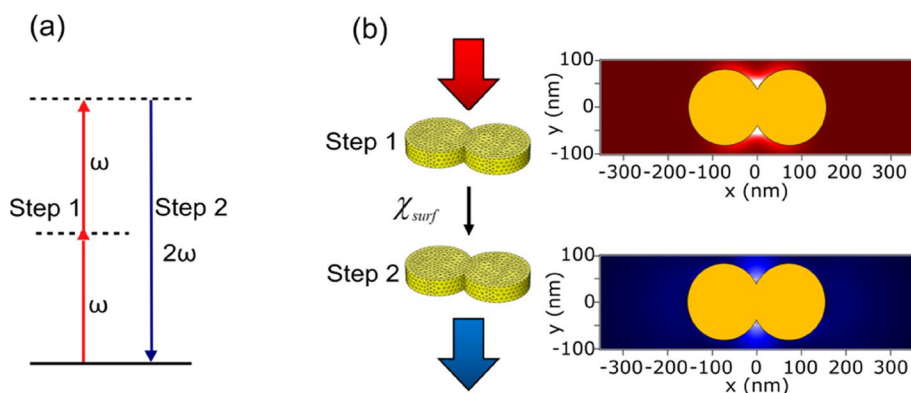
Fig. 1 SHG principles. **a** Energy level diagram for SHG. SHG is a parametric process involving virtual states (indicated as dashed horizontal lines), corresponding to the destruction of two fundamental photons followed by the generation of one SH photon. **b** Classical description of SHG. The fundamental near field driven by the incoming wave induces a nonlinear surface polarization $P_{surf,n}(\mathbf{r}, 2\omega)$ due to the nonlinear surface susceptibility χ_{surf} (step 1). The second step is the electromagnetic radiation of the nonlinear sources. Reprinted with permission from The Journal of Physical Chemistry C 2016, 120, 17699–17710. Copyright 2016 American Chemical Society

The non-zero independent elements decrease considering the surface symmetry. Among different contributions, the normal component of the surface polarization $\mathbf{P}_{surf, \perp}(r, 2\omega)$ induced by the $\boldsymbol{\chi}_{surf, \perp\perp\perp}$ (where $\perp$ denotes the component normal to the surface) of the surface tensor becomes dominant for SHG from plasmonic nanostructures [15, 60]. Other contributions, such as tangential components of the surface tensor, contribute weakly to total SH responses [3]. The local nonlinear polarization can be simplified as [15, 74]:

$$P_{surf,\perp}(2\omega) = \boldsymbol{\chi}_{surf,\perp\perp\perp}E_n(\omega)E_n(\omega) \tag{1}$$

The nonlinear emission in SH frequency can then be quantified by using the Lorentz reciprocity theorem [84]:

$$E_{nl}(2\omega) \propto \int\int P_{surf,\perp}(2\omega) \cdot E_n(2\omega)ds \tag{2}$$

where $E_n(2\omega)$ is the nonlinear mode at the SH frequency normal to the surface of the nanostructure.

From the above equations, potential factors that induce a strong SHG emission at least include: a) Nonlinear materials with high$\chi_{surf,\perp\perp\perp}$; b)A highly localized electric field at both fundamental ($E_n(\omega)$) and second harmonic ($E_n(2\omega)$) frequencies; c) Constructive interference between the nonlinear polarization mode and its harmonics, which plays a crucial role during the propagating process of SHG signals from the near-field to far-field [84]. For the nonlinear materials, we will focus on the plasmonic metals, Au in particular ($\chi_{surf,\perp\perp\perp} \approx 2.3 \times 10^{-13}$ cm^2/statvolt at the pump wavelength of 800 nm [3]), due to their strong and tunable plasmonic responses and ease of fabrications. Hereafter we systematically investigate the following influencing factors leading to a strong SHG radiation: local electric field enhancement taken in charge by resonance effect and mode matching at SH frequency.

Resonance effect

We firstly consider the influence of resonance effect. When the electromagnetic wave interacts with a metallic nanostructure, the local field could be strongly enhanced by matching the oscillating frequency of the fundamental laser field or higher order harmonic fields to the plasmonic resonance. The conversion yield of nonlinear optical processes, which varies nonlinearly with the fundamental intensity, might increase with the fourth or a higher power with the local field factor L(ω) evaluated at the fundamental frequency [15]. The plasmon enhanced SHG was reported in 1974, in which the reflected SHG intensity increased by several orders of magnitude when the incident angle allowed surface plasmon polaritons propagate on a silver film [3, 80]. Since this effect was observed, it has become a well-known strategy to boost nonlinear optical effects, SHG in particular, of plasmonic nanostructures up to date [19, 73, 85, 86]. Here, we are trying to use a phenomenological model to quantify the SHG enhancement induced by resonance effect at the fundamental laser field, and then expand the model to higher orders of driving field.

Resonance effect at the fundamental frequency

When a metallic NP is excited by an optical field, the induced polarization can be analogically regarded as mechanical vibrations under a periodic driving force for a damped single degree-of-freedom system [27]. The Lorentzian oscillator in electromagnetism is basically a special application based on such a classical vibration theory, where the driving force F is replaced by electric force $-eE(t)$. Such a mechanical analogue is necessary to better understand the resonant excitation, the driving amplitude and phase during light-matter interactions and especially the couplings between two or more NPs.

The unperturbed Lorentzian model can be expressed as:

$$\ddot{x} + 2\gamma\dot{x} + \omega_0^2 x = -\frac{e}{m}E(t) \tag{3}$$

where x(t) represents the electron oscillating displacement, γ indicates the system damping, $\omega_0 = \sqrt{k/m}$ is the resonance frequency, e and m are the electron charge and mass, respectively. The solution in frequency domain is given by [73]:

$$x(\omega) = -\frac{e}{m}g(\omega)E(\omega) \tag{4}$$

where $g(\omega) = -(\omega^2 - \omega_0^2 + 2i\gamma\omega)^{-1}$ is the linear response function of the Lorentzian oscillator. The local field enhancement factor in fundamental frequency L(ω) is proportional to the absolute value of g(ω) [73, 87]. Therefore, the plasmonic resonance with a peak position that is closer to the fundamental excitation or with a sharper linewidth results in a stronger L(ω). The recent study introduced a resonant excitation factor (REF) to quantify this effect [19]:

$$REF(\omega, \gamma) = \frac{\frac{\gamma}{2\pi}}{\left[(\omega - \omega_0)^2 + \left(\frac{\gamma}{2}\right)^2\right]} \tag{5}$$

where $\gamma = \gamma_0 + \Delta\gamma$. The term γ_0 denotes the damping constant of free electrons, which is determined by material properties. $\Delta\gamma$ denotes the lifetime of plasmonic mode, which can be characterized by the full-width at half maximum (FWHM) of the resonance. If spectral linewidth broadening is neglected, a resonance profile approaches a delta function [88]. In this case, $\Delta\gamma$ approaches zero, and the system damping is only determined by the material properties [19].

For plasmonic NPs, taking a nanosphere for example, the resonance frequency ω_0 could be evaluated in quasi-static approximation if Fröhlich condition is satisfied for the polarization:

$$P = 4\pi\varepsilon_0\varepsilon_m a^3 \frac{\varepsilon - \varepsilon_m}{\varepsilon + 2\varepsilon_m} \mathbf{E}_0 \tag{6}$$

where ε_0, ε and ε_m is the permittivity of the free space, metal nanosphere and surrounding medium, respectively. a is the radius of the nanosphere. $\mathbf{E}_0$ is the incidence electric field. As can be seen from Eq. (6), when the denominator of the linear polarization approaches zero, a resonant enhancement would appear at a certain optical frequency (ω_0).

Figure 2a shows the scattering spectra of Au nanodiscs with varying diameters. As the diameter of Au nanodisc increases from 80 to 200 nm, the dipolar plasmonic mode red
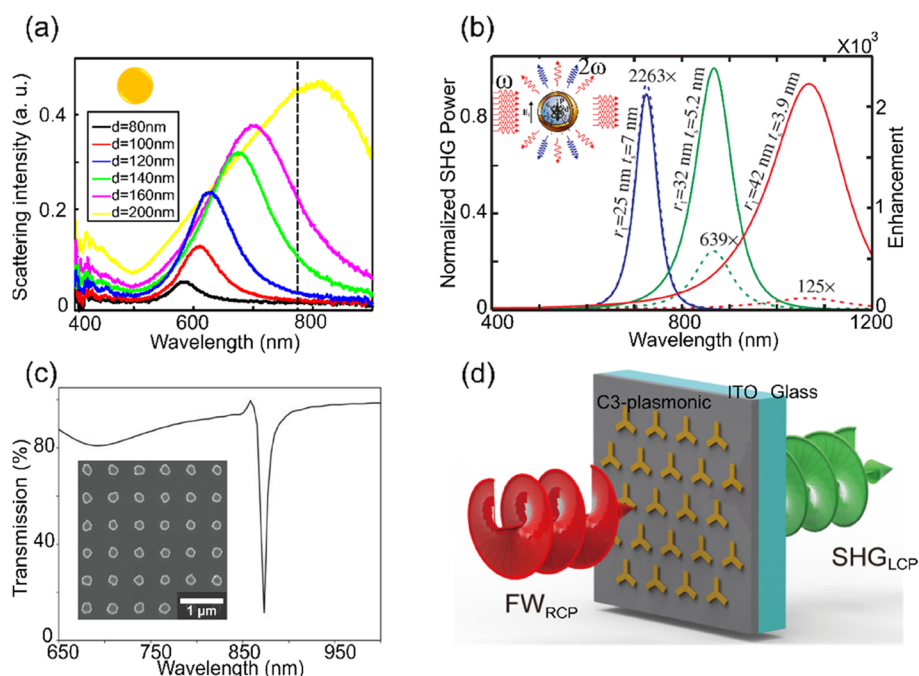
Fig. 2 Resonance effect at the fundamental frequency. **a** The scattering spectra for single Au NPs with varying disc diameters. The dashed black line represents the fundamental wavelength 778 nm. Reprinted with permission from Nanoscale 2019, 11, 23,475–23,481. Copyright 2019 Royal Society of Chemistry. **b** SHG enhancement is achieved by matching the fundamental wavelength to the plasmonic resonance of a BaTiO3@Au core–shell nanocavity. Reprinted with permission from Physical Review Letters 2010, 104 (20), 207,402. Copyright 2010 American Physical Society. **c** SHG enhancement is achieved by matching the fundamental wavelength to the surface lattice resonance. Reprinted with permission from Nano Letters 2019, 19, 165 − 172. Copyright 2019 American Chemical Society. **d** SHG enhancement is achieved by matching the fundamental wavelength to the epsilon-near-zero wavelength of ITO layer. Reprinted with permission from Nano Letters 2020, 20, 7, 5421–5427. Copyright 2020 American Chemical Society

shifts from ∼ 580 nm to ∼ 800 nm [19]. Wang et al. found that strong SHG intensity can be obtained if the LSPR of Au nanodisc was approaching to the fundamental wavelength (dashed vertical lines) [19]. They calculated REFs in accordance with Eq. (5), which agree very well with experimental results of SHG emission intensity, validating such a simple but sufficiently precise model to design efficient SHG emitters.

Plasmonic NPs are also used to enhance the SHG radiation of traditional nonlinear crystals. For example, as shown in the inset of Fig. 2b, Pu et al. used BaTiO3@Au core–shell nanostructures to enhance the radiation of SHG [89]. By tuning the diameter of the core and the thickness of shell, plasmonic resonances of such stratified nanostrucutres can be tuned in a broad wavelength band. As shown in Fig. 2b, by matching fundamental excitations with plasmonic resonances, an experimental enhancement of over 500 times in the SH radiation power was achievable [89].

From the Eq. (5), it is also found that a sharper resonance at the fundamental excitation wavelength leads to a stronger resonance effect. People also try to find the resonances with higher figure of meris (FoM) to obtain larger enhancement factors of SHG. Surface lattice resonances (SLRs) coupling the LSPRs with the Rayleigh Anomaly are introduced to enhance the radiation of SHG [90–92]. The FoM of SLRs is always is more than one order of magnitude larger than that of pure LSPRs [93] The resonance position

can be tuned by varying the lattice constant or the incidence angle. As shown in Fig. 2c, by patterning the Au nanodiscs in an array with a period of 600 nm, a sharp SLR locating at 872 nm can be found from the transmission spectra [91]. By tuning the fundamental wavelength and incidence angle, Hooper et al. enhanced the SHG signal by up to 450 times [91].

Besides, it is recently found that strong local field enhancement can be achieved at or near the epsilon-near-zero (ENZ) wavelength, at which the real part of the permittivity switches from a positive to a negative value [94]. ENZ behaviors are observed at the onset of a plasmonic response in metals or highly doped semiconductors [95, 96]. Indium-tin oxide (ITO) and aluminium-doped zinc oxide are among the most investigated ENZ materials. By coupling the C3 plasmonic metasurfaces with an ITO layer, as shown in Fig. 2d, Deng et al. observed an approximately 104-fold experimentally measured SHG enhancement at normal incidence at the fundamental wavelength near the ENZ condition of ITO [96].

Resonance effect can not only enhance the SHG, but also other higher harmonic generations from plasmonic nanostructures. Taking THG for instance, as shown in Fig. 3, experimental THG intensities excited by different fundamental laser wavelengths generally follow the tendencies of their linear extinction spectra [87]. This supplies further evidences to the
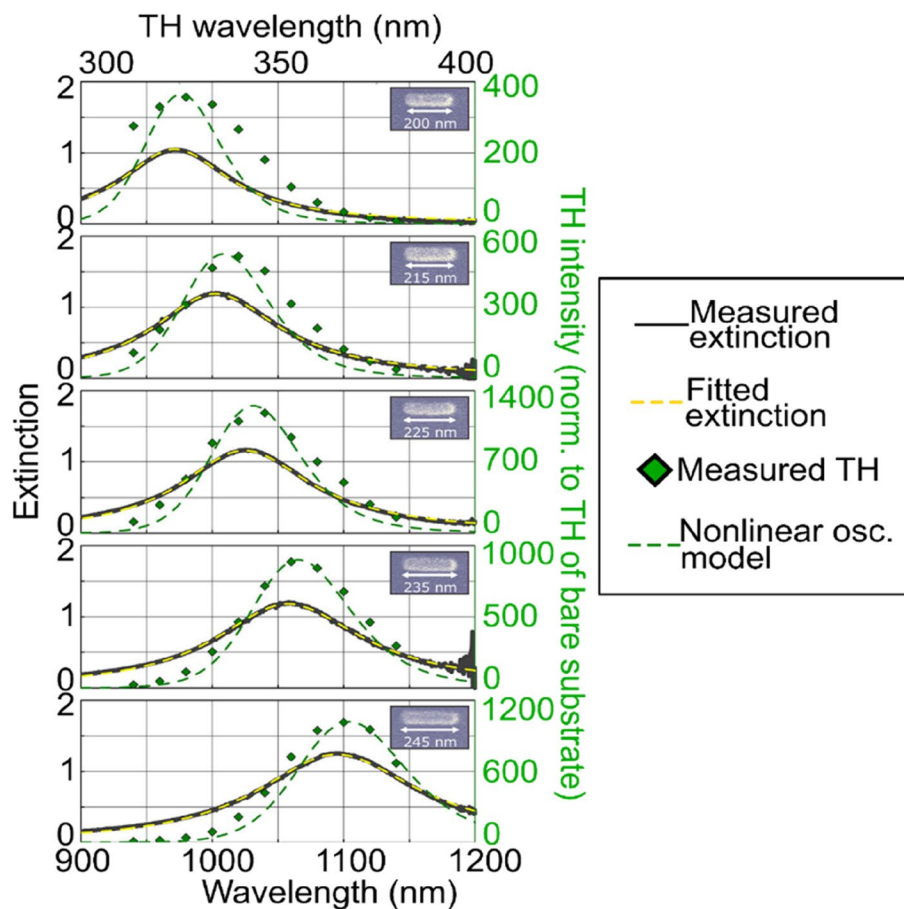
Fig. 3 Third-harmonic generation intensities follow the tendencies of plasmonic resonances. Reprinted with permission from Optics Letters 2012, 37, 4741–4743. Copyright 2012 Optical Society of American

predominant role of fundamental local fields in far-field intensities of coherent nonlinear optical signals.

Resonance effect at the high-order harmonics

The unperturbed Lorentzian model used above quantifying resonance effect simply neglects nonlinear terms supported by high-order driving frequencies, e.g., second- or third-harmonic excitations. It is, however, worth noting that matching plasmonic resonances to the second-harmonic frequency can also lead to a strong SHG radiation. As reported by Bernd Metzger et. al. [97], far-field SHG intensities excited by various laser wavelengths clearly follow the plasmonic resonances presented at their SH frequencies, see Figs 4a ~ b.

A phenomenological model based on the Lorentzian oscillator was proposed [73]:

$$I^{(2)}(2\omega) \propto \omega^2 \left| L(2\omega)L(\omega)^2 \right|^2 \tag{7}$$
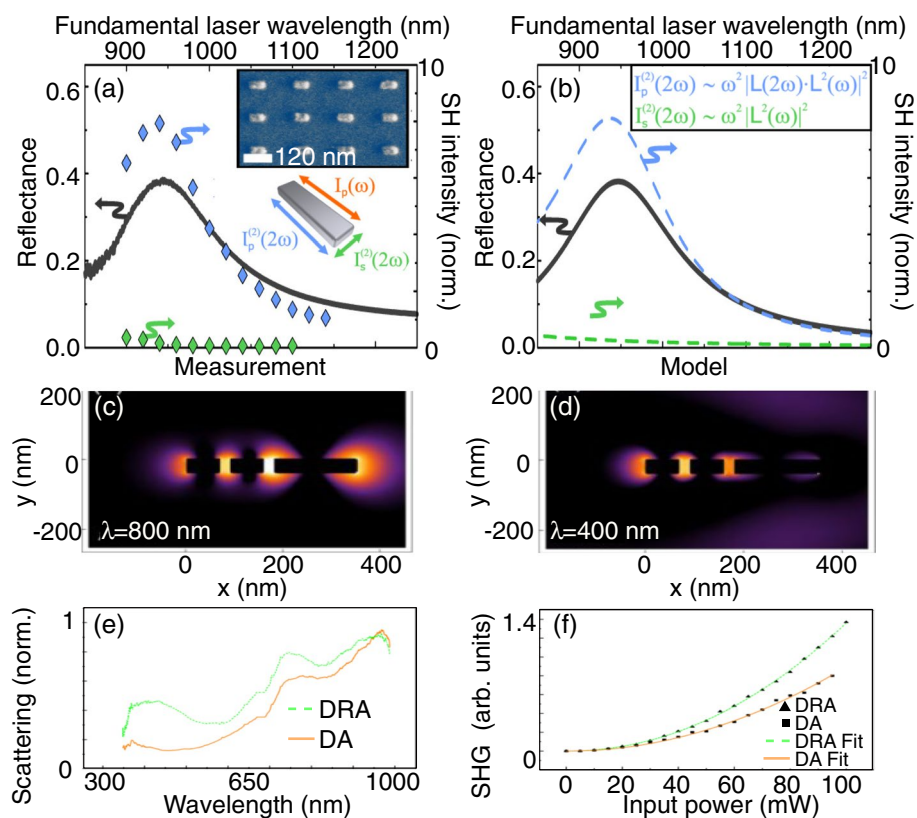
Fig. 4 Resonance oscillating effect by matching plasmonic resonances to second-harmonic wavelengths. (a ~ b) Experimental (**a**) and modeled (**b**) polarization-resolved SHG spectra together with corresponding reflectance spectra of Al nanorod arrays. The black solid lines are reflectance spectra, the blue and green curves are the SH spectra in p- and s-polarized light, respectively. Reprinted with permission from Nano Letters 2015, 15, 3917 – 3922. Copyright 2016 American Chemical Society. **c-f** Double resonant nanoantennas. The electric field distributions at the fundamental (**c**) and second-harmonic wavelength **d**. The scattering spectra (**e**) and SHG intensity (**f**) are compared between double resonant antenna (DRA) and dipole antenna (DA). Reprinted with permission from Optics express 2012, 20, 12,860–12865. Copyright 2012 Optical Society of American

where $I^{(2)}(2\omega)$ is far-field SHG intensity using p-polarized light, L(2ω) and L(ω) are local field enhancements due to SH and fundamental driving fields, respectively. As proposed by Bernd Metzger et. al., L(2ω) for plasmonic nanorods can be evaluated by

$$L^{(2)}(2\omega) \propto \frac{I_p^{(2)}(2\omega)}{I_s^{(2)}(2\omega)} \tag{8}$$

where $I_p^{(2)}(2\omega)$, $I_s^{(2)}(2\omega)$ are SHG intensity using *p-* and *s-*polarized light, respectively. For the plasmonic nanostructures with other shapes, p-polarized light can be generalized to a light inducing a plasmonic resonance near the SH excitation, while s-polarized light inducing none plasmonic resonance near the SH excitation or a plasmonic resonance far from SH excitation.

As shown in Eq. (7), the SHG intensity is not only determined by the local field enhancement at the fundamental frequency L(ω), but also the SH frequency L(2ω). Thus, an optimal idea is to design multiple plasmonic resonances matching both the fundamental and other high orders of driving frequencies, which are referred to as double or multiple resonant nanoantennas. As shown in Fig. 4c~f, a nanostructure consists of three nanorods with 20 nm of nanogaps has plasmonic resonances at both fundamental (800 nm) and SH wavelength (400 nm) [98]. The experimental results confirm that such a double resonant antenna (DRA) emits a stronger SHG than that of a simple dipole antenna (DA) with only a resonance at fundamental wavelength. Similar studies report that matching the longitudinal and transverse dipolar plasmonic resonances of Ag-coated LiNbO$_3$ core–shell nanocuboids to the fundamental and SH wavelengths shows a giant enhancement of SHG by a factor of 3×10^5 in comparison to the case of matching only a single plasmonic resonance [99].

Similar improvements of SHG could be achieved by matching the fundamental or higher-order driving fields to other kinds of resonances, e. g. Fano resonance [60, 100], magnetic resonance [101] and so on. Taking the Fano resonance for example, Thyagarajan et. al. showed that SHG benefited from the presence of Fano resonance at the fundamental wavelength in a multiple resonant nanoantennas, see Fig. 5a [60]. By matching the Fano dip at 800 nm and another scattering peak at 400 nm, the silver haptamer obtained 3 times stronger of SHG under the Fano resonance excitation (blue curve) than that of mere dipolar resonance excitation (violet curve), as shown in Fig. 5b. Alternatively, Chandrasekar et. al. designed a plasmonic metasurface consisting of coupled silver nanostrips gratings, and aligned its magnetic and electric resonances in fundamental and second-harmonic frequencies, respectively, as can be seen in Fig. 5c~d [101]. The SH conversion efficiency of such nanostructure reached 1.32×10^{-10}, which was increased by around 30% in comparison with mere matching the only electric resonance.

Mode matching

Symmetry breaking

Stronger SHG emissions are normally observed by breaking the centrosymmetry of nanostructures.For example, split-ring resonators has led to a substantial SHG enhancement, due to large field confinements associated with magnetic resonances and potential changes of second-order nonlinear-optical susceptibility [102, 103]. Other non-centrosymmetric shapes such as chiral G-shaped nanostructures [104, 105], L-shaped
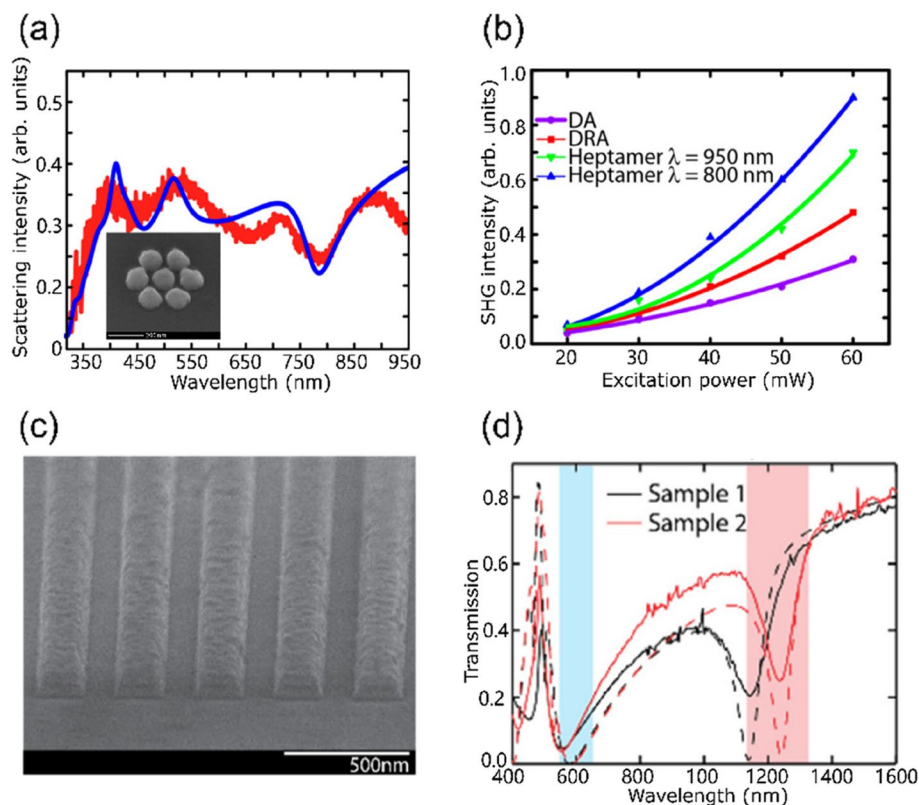
Fig. 5 Matching the fundamental and SH driving fields to Fano (a ~ b) and magnetic field (c ~ d) resonances to enhance the SHG radiation. **a** Experimental (red) and simulated (blue) scattering spectra of a silver haptamer. The inset shows the SEM image. **b** SHG intensity comparisons among a dipole antenna (DA), a double resonant antenna (DRA), a haptamer excited at the fundamental wavelengths of 950 nm and 800 nm. Reprinted with permission from Nano Letters 2013, 13, 1847 − 185. Copyright 2013 American Chemical Society. **c** SEM image of coupled silver nanostrips gratings. **d** Experimental (solid) and simulated (dashed) transmission spectra for sample 1 and 2. Reprinted with permission from Optical Materials Express 2015, 5(11), 2682–2691. Copyright 2015 Optical Society of American

nanostructures [106], T-shaped Au nanostructures [107] and nanoholes in metallic films [108, 109] were designed to improve SHG radiations based on different principles, as shown in Fig. 6a ~ d. In general, a symmetry-breaking nanostructure would allow higher net dipole modes and constructive overlapping between the linear modes and nonlinear modes, giving rise to a higher SHG emission in the far field [84].

The symmetry breaking could also be achieved by using so called heterodimers, in which two constituting nanoantennas are made of different materials and closing to each other by a subwavelength nanogap. Benefiting from both advantages of asymmetry and nanogaps, a heterodimer becomes an attractive option of being SHG emitter. Wang et. al. achieved extremly strong SHG intensity from Au-Al heterodimers by precisely controlling the size and gap of NPs [19], As shown in Fig. 6e. They compared the SHG emission among three kinds of nanoantennas which have the same size of NPs: an Al monomer, an Au monomer and an Au-Al heterodimer. They found that Au-Al heterodimer has the strongest SHG emission. SHG intensity of Au-Al heterodimer is even stronger than the sum of those of the individual Au and Al NPs. One of obvious strategies they used is that such an Au-Al heterodimer was served as a
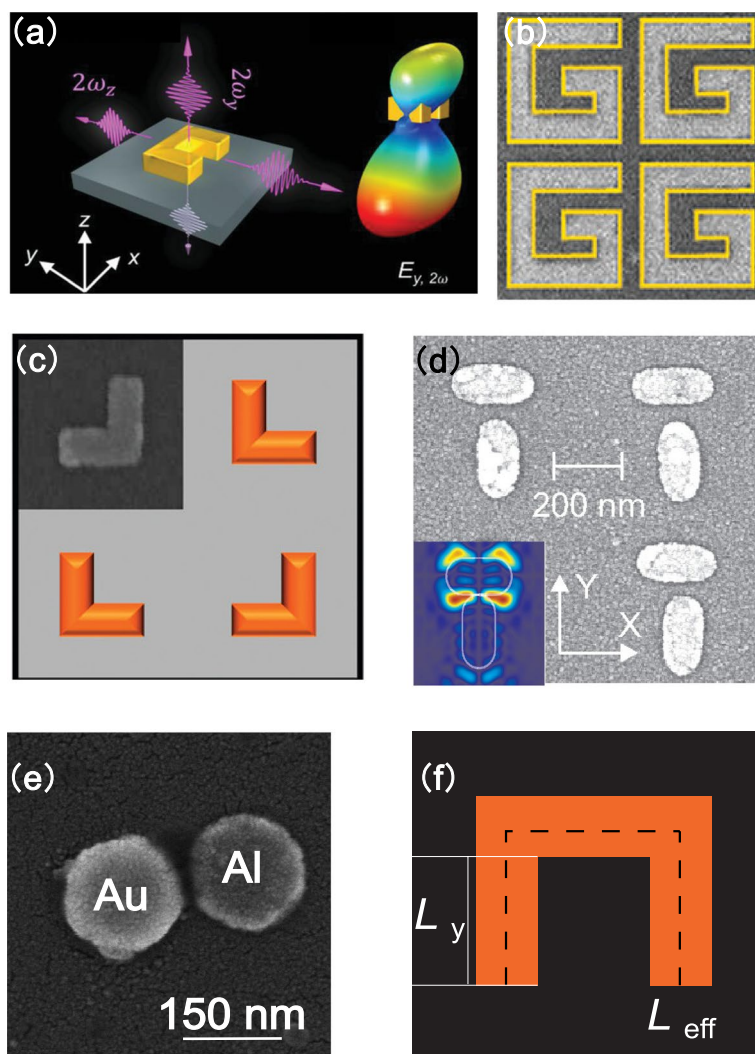
Fig.6 SHG emission from noncentrosymmetric nanostructures. The split-ring (**a**, **f**) chiral G-shaped (**b**), L-shaped (**c**), T-shaped (**d**) and single Au-Al heterodimer (**e**) nanostructures were used to enhance the SHG emissions. Reprinted with permission from Advanced Materials 2019, 31, e1806479 (**a**), Nano Letters 2009, 9, 3945–3948 (**b**), Nano Letters 2012, 12, 673–677 (**c**), Nano Letters 2007, 7, 1251–1255 (**d**), Nanoscale 2019, 11, 23,475–23,481 (**e**). Copyright 2019 Wiley–VCH GmbH; 2009, 2012, 2007 American Chemical Society; 2019 Royal Society of Chemistry

DRA, in which a dipolar-dipolar coupled plasmon mode and a quadrupolar-quadrupolar-like coupled plasmon mode of Au-Al heterodimer matched the fundamental and second-harmonic excitations, respectively [19].

To quantify the influence of geometric asymmetry on the nonlinear polarization and thus SHG emission. O'Brien K et al. defined a parameter of asymmetry ratio R [84]. Taking the "U"-shaped nanoantenna for example, as shown in the inset of Fig. 6f, R equals to L_y/L_{eff}. In their experiments, they observed the maximum SHG emission corresponds to an asymmetry ration $R = 0.18 \pm 0.02$, as shown in Fig. 6f, which was then predicted by using a nonlinear scattering theory.

Mode / phase interference

It is worth noting that neither a noncentrosymmetric shape nor a strong localized fundamental field necessarily definitely result in a strong SHG radiation in the far-field. Essential impacting factor should include constructive interference between the nonlinear polarization mode and its harmonics. Mode interference issues are aroused from an interesting phenomenon: although strong electromagnetic field enhancements at the fundamental or SH frequency can be observed from so called 'hot spots', e.g., in the nanogap of two constituting NPs, far-field SHG intensity becomes extinct in some cases. Bouhelier et. al. observed so called SHG silencing effect by using three optical gap antennnas with the gap values of 0, 15 nm and 70 nm, as can be seen from Fig. 7a [110]. Interestingly they found that the nanoantenna with the gap size of 70 nm radiated a stronger SHG in the gap region than the one with a gap size of 15 nm, as shown in Fig. 7b. Further simulations revealed the fact that although there were extreme stronger confinements of electric field in the gap of the nanoantenna with a gap of 15 nm, polarization vectors at each side of the nanogap were out of phase and their contributions to the far-field SH wave tent to cancel each other out, as can be seen from Fig. 7c ~ d. The destructive interference finally resulted in a limited far-field SH signal.

In their following work [111], the same research group observed remote emission of two-photon luminescence and SHG from micrometer-long nanorods at the opposite side of local illumination, regardless of a central gap, as shown in Fig. 7e. The gap between two nanorods otherwise allows the coupling and propagation of excited surface
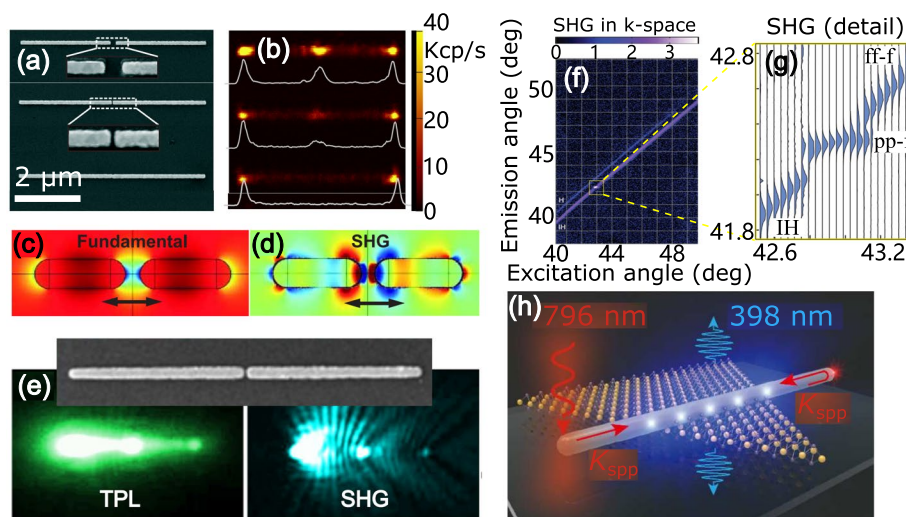
Fig.7 Mode or phase matching at the SH frequency. SEM images (**a**) and optical images at SH wavelength (**b**) of three gap antennnas with the gap values of 0, 15 nm and 70 nm from the bottom to top. **c, d** show the electric field distributions of the gap antennas with the gap value of 15 nm at the fundamental and SH wavelengths, respectively. Reprinted with permission from Optics Express 2012, 20, 10,498–10508. Copyright 2012 Optical Society of American. **e** Remote excitation of SHG and TPL of Au gapped nanorods through excitation of surface plasmons. Reprinted with permission from Physical Review Letters 2015, 115, 19,740. Copyright 2015 American Physical Society. **f, g** An SH photon was created by annihilating two copropagating surface plasmons. Reprinted with permission from Physical Review Letters 2012, 108, 136,802. Copyright 2012 American Physical Society. **h** An SH photon was created by annihilating two counterpropagating surface plasmons. Reprinted with permission from Nano Letters 2017, 17(12), 7803–7808. Copyright 2017 American Chemical Society

plasmons. They confirmed that constructive surface plasmon mode developing in the antenna carries enough energy to produce a distributed nonlinear response during its propagation.

A more systematical picture of surface plasmon-induced SHG could be found from the work of Grosse N B et al. [112]. They employed k-space spectroscopy in the Kretschmann geometry, to examine the emitted SHG in a way that provides precise information on surface plasmon nonlinear phase-matching. As shown in Fig. 7f, g, in addition to two channels where an SH photon (both homogeneous 'H' and inhomogeneous 'IH') is generated by two fundamental photons (ff-f), they observed another even more significant channel where two copropagating surface plasmons annihilate to create an SH photon (pp-f). Besides of using copropagating surface plasmons, Li Y et al. found that SH photons could be created perpendicular to an Ag nanowire where two surface plasmons are counterpropagating and annihilated, as shown in Fig. 7h [113].

In summary, mode (for localized systems) or phase (for propagating systems) matching is essential for the process of two surface plasmons annihilating and generating one SH photon. This matching condition ensures conservation of energy and momentum while optimizing the interference and coupling between plasmons by tuning incidence or geometric parameters. Phase-matched surface plasmons thus provide another efficient route to converse the fundamental photons into SH photons.

MPL

The metallic photoluminescence was first observed by Mooradian from bulk copper and Au in 1969 [35]. In his experiment, excited by a 488 nm monochromatic light, a broad peak centered near the interband absorption edge was observed. The emission peak was attributed to direct radiative recombinations of electrons near the Fermi level with holes in the first d-band. Due to the high density-of-state, interband transitions would preferentially take place near specific symmetry points of the Brillouin zone [36, 114]. Rosei developed quantitative models to calculate inter-conduction-band transitions involving Fermi surface [115–118]. G. T. Boyd et. al. measured one-photon and multiphoton-induced luminescence from silver, copper and gold films with both smooth and rough surfaces [36]. A classical model combining Fresnel coefficients and Rosei's interband transitions was put forward to calculate photoluminescence intensity for smooth metallic films [36, 118]. With respect to rough films, Fresnel factors were corrected by macroscopic local-field factors, where rough surfaces were modelled as hemispheroids locating on smooth metallic films [36].

Metallic photoluminescence is generally described as a three-step process, as shown in Fig. 8a. (1) Excitation stage. An electron from the ground state is promoted to the excited state by absorbing one (leading to OPL) or more photons (leading to MPL), leaving a hole behind. (2) Relaxation stage. Excited electrons arrive at the emission state if a thermal equilibrium is achieved via electron–electron, and electron–phonon scatterings [119, 120]. (3) Emission stage. The electrons in the emitting state recombine with the holes in the ground state in step (1), either radiatively in terms of photoluminescence (solid arrow) or non-radiatively in terms of heat dissipation (dashed arrow) [15]. Hereafter we take TPL as an example to discuss the three stages of metallic photoluminescence in details.
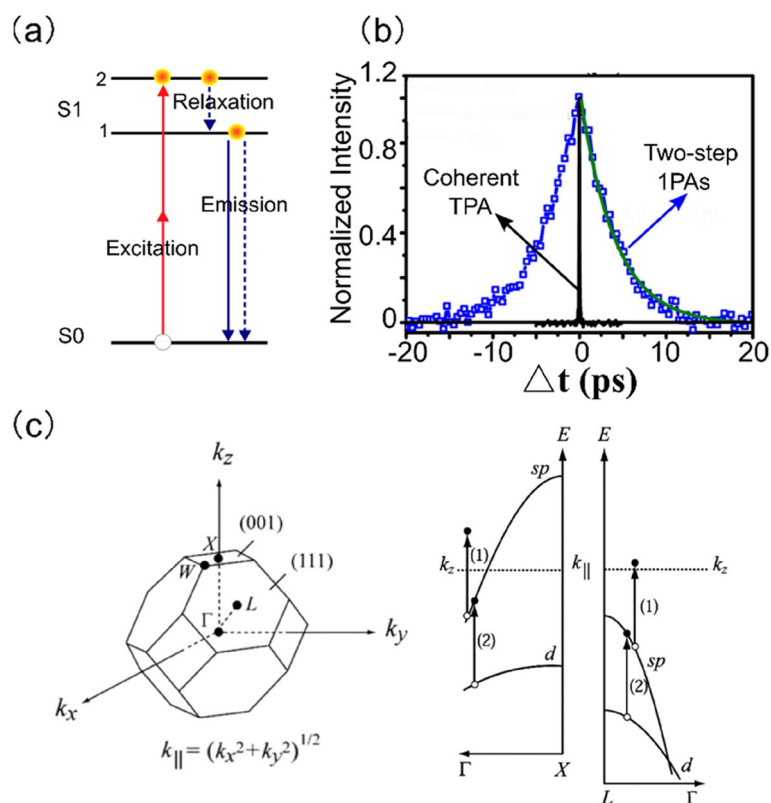
Fig. 8 Physical mechanisms of TPL excitation and emission. **a** A complete TPL process consists of three steps: namely excitation step ①, relaxation step ② and emission step ③. │g>, │e1>, │e2>represent the ground stage, the excited state and the emission state, respectively. Reprinted with permission from The Journal of Physical Chemistry C 2016, 120, 17,699–17,710. Copyright 2016 American Chemical Society. **b** Two physical mechanisms to describe the excitation process of TPL are clarified by using autocorrelation experiments. Reprinted with permission from The Journal of Physical Chemistry Letters 2013, 4, 1634–1638. Copyright 2013 American Chemical Society. **c** Two sequential one-photon absorption (1PA) processed occurs near the symmetry points of X and L of the first Brillouin zone of gold. Reprinted with permission from The Journal of Physical Chemistry B 2005, 109, 13,214–13,220. Copyright 2005 American Chemical Society
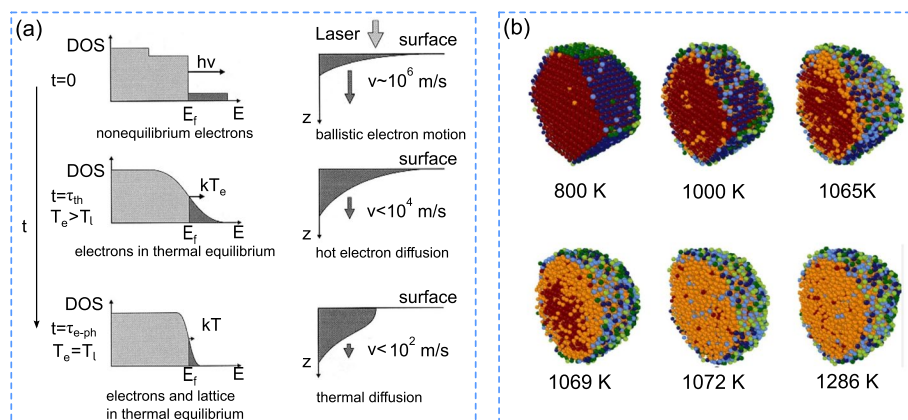
Excitation process

The excitation process of metallic photoluminescence is generally described by using a two-photon absorption (TPA) process. In such a physical model, electrons in the ground state absorb two photons simultaneously through a virtual intermediate state and are finally excited to an excited state. In the time domain, ideally there is no delay between the two absorbed photons. This description fits well with the classical nonlinear optics and is largely accepted in theoretical calculations [15, 36].

However, more and more experimental investigations evidence that the absorbing of two photons is incoherent, in which two sequential one-photon absorption steps through real intermediate states are involved. For instance, Xiaofang Jiang et. al demonstrated that in gold nanorods the excitation process arised from two sequential one-photon absorptions by power dependence measurements, as it is shown in Fig. 8b [121]. Taking gold for instance, two sequential one-photon absorptions (1PAs) are further understood that the first photon is absorbed by sp electron below Fermi level E_f, which is followed by intraband transitions and excitation to the state above E_f. The second

photon is absorbed by the d band electron, which is then excited to the sp band through interband transitions. These sequential processes finally create holes in d band and electrons in sp band. The whole process can be illustrated through Fig. 8c, which shows the intraband transition (step 1) and interband (step 2) transition of electrons near symmetry points of X and L of the first Brillouin zone of gold, due to their high joint density of states [36, 37, 114, 116]. Two sequential 1PA steps model taking the real energy bands of metals into account become more and more accepted in the recent studies [36, 37, 43, 114, 122].

Relaxation

As a luminescent process, the excited electrons are not simultaneously emitting photons at the excited states, but it undergoes a time-dependent relaxation process. In such a process, nonequilibrium hot electrons become gradually equilibrium and transfer energies to the deeper electrons and lattices through electron–electron and electron–phonon scattering processes. In according to Hohlfeld's description, the relaxation process is divided into three intervals in time sequence, as it is shown in Fig. 9a [119] At the first stage, the electron distribution becomes highly nonequilibrium immediately after the laser excitation. The hot electrons move to deeper surface with velocities close to the Fermi velocity and develop the temperature to the electrons around the Fermi level through electron–electron collisions. At the second stage, a thermal equilibrium among hot electrons is reached. The electron distribution follows a Fermi–Dirac function. At the meantime, driven by the temperature gradient, the hot electrons diffuse the thermal energy to the deeper bulk through electron–phonon couplings. The diffusion dynamics can be described by the two-temperature model. At the last stage, the electrons and

Fig. 9 Transient electron and atom temperature distributions in the Photoluminescence relaxation process. **a** Three relaxation stages of optically excited electrons. T_e and T_l represent the temperature of electrons and lattice, respectively. τ_{th} and τ_{e-ph} are the time of electron–electron scatterings and electron–phonon couplings, respectively. Reprinted with permission from Chemical Physics 2000, 251, 237–258. Copyright 2000 Elsevier Publishing Group. **b** Snapshots of Au 6266 simulated using the revised Perdew-Burke-Ernzerh machine-learning force fields (rPBE ML-FF) at different nominal simulation temperatures, with atoms coloured according to the clustering algorithm. Red: solid inner; yellow: liquid inner; dark blue: solid high-coordination surface; light blue: liquid high-coordination surface; dark green: solid low-coordination surface; light green: liquid low-coordination surface. Reprinted with permission from Nature Communications 2021, 12, 6056. Copyright 2021 Springer Nature Publishing Group

the lattices reach thermal equilibrium. The temperature of local hot spots would further decrease due to the thermal diffusions to cooler lattices and the ambient.

One inevitable topic in this process is the thermal damage, considering relatively low melting points of metallic nanostructures. The criterion of thermal damages could be that thermalized lattice temperature becomes equal to the melting point of nanostructures. The lattice temperature dynamics of the bulk material can be usually described by the two-temperature model or more precise three- temperature model, taking the thermal diffusions from the lattices to the ambient into account. Now the key issue turns to how to quantify the thermal dynamics of the plasmonic NPs, since there are significant differences from macroscopic ones. One widely adopted solution is molecular dynamic method, which simulates the atomic motion based on the Newtonic mechanics. For example, Wang et. al. combined molecule dynamics and the two-temperature model to simulate ultrafast laser interaction with free gold NPs with sizes 2.44 ~ 6.14 nm (up to 7164 atoms) [123]. Zeni et. al. combined interpretable machine learning force fields with molecule dynamics to investigate the thermodynamic stability of gold NPs of different sizes (1 to 6 nm), containing up to 6266 atoms [124]. Figure 9b shows their simulations on the phase evolution of a gold NP containing 6266 atoms at different nominal temperatures. As we can see, with the temperature increases, the liquid phase atoms increase from the surface to the center of mass. Wang et. al. used molecule dynamics simulation to analyze the coalescence of two gold NPs [125]. The simulation results were in good agreement with the experimental results.

Emission

When thermalized electrons relaxed to the emission state, the metallic photoluminescence is ready to generate. Classical description attributes MPL emission to recombinations of excited electrons in the higher conduction bands (above the Fermi level E_{fl}) and holes in the lower valence bands. The emission spectral profile is thus mainly determined by intrinsic material properties, e. g. the energy bands [36, 37, 114]. This mechanism successfully explains the most experimental results from metallic films or bulk crystals [35, 36, 114]. For instance, Boyd et. al. predicted the emission spectra of TPL for the rough films of bulk gold, Cu and Ag, considering the electron–hole recombination near the L symmetric points between 6–5 bands and 6–4 bands [36].

It is known that roughened surfaces usually lead to strong metallic photoluminescence due to lightning rod effects, or local field enhancements supported by particle plasmons (PPs) [36]. Similar to surface enhanced fluorescence spectroscopy, PPs in the emission of metallic photoluminescence is generally regarded to be a supplier for strong local field enhancement, which alters radiative and non-radiative decay rates during the electron–hole recombination [36, 126–128]. This is also the reason why the investigations on NPs becomes more and more of importance due to dependences of PPs on individual shapes, sizes, and dielectric environment. T. V. Shahbazyan et. al established a model for calculating plasmon-assisted metallic photoluminescence from the view of quantum field theory [128]. In his theory, the local field enhancement derives not only from the surface plasmons, which are the collective excitations of conduction band electrons, but also from the excitations of d-band holes through Auger scatterings [128, 129].

Nevertheless, more and more studies evidence that the spectral shape and energy of metallic photoluminescence closely follow the scattering or extinction spectra of NPs, which clearly demonstrates the fingerprints of PPs [15, 37, 120]. The emission of metallic photoluminescence is then attributed to the radiative decay through energy levels of PPs [37, 43, 122, 130]. The PPs modulated OPL was firstly observed by Dulkeith E. et. al. from the gold NPs [130]. A photoluminescence efficiency of 10^{-6} which is four orders of magnitude higher than the one from metal films was found. They attributed such efficient metallic photoluminescence to radiative decay of PPs, which are generated by the nonradiative recombination of d-band holes and sp electrons [130]. Hu H. et. al. compared the OPL with the corresponding scattering spectra using lithographically defined gold nanostructures [120]. They found that OPL has similar spectral profiles but with a reproducible blue shift of peak positions to the corresponding scattering spectra, as shown in Fig. 10a. Fang Y. et. Al [131]. (Fig. 10b) and Wackenhut F. et. Al [43] reported that the OPL from gold nanorods closely resemble to the scattering spectra. They assigned metallic photoluminescence to the radiative decay of longitudinal surface plasmons generated after fast interconversion from either the transverse surface plasmons or electron–hole pairs. Similar to OPL, Horneber A. et. Al [122] and Wang J. et. Al [15] observed PPs-like emission spectra of TPL from gold nanoparticles. They attributed the metallic TPL to the radiative decay of thermalized electrons from the plasmon energy states.

An alternative interpretation of metallic photoluminescence might derive from both physical mechanisms, namely carrier recombination and plasmon emission channels. By comparing the emission spectra of gold NPs of varying sizes with the corresponding dark-field scattering spectra, Wang J. et. al. observed two nearly static emission modes and one shifting emission mode, as shown in Fig. 10c [37]. They attributed the static modes to the emission of radiative decay of electron–hole pairs, and the shifting mode to the emission of radiative decay of PPs [37]. A new physical mechanism was proposed as shown in Fig. 10d. The excited electrons and holes either recombine radiatively in terms of photons (①) or non-radiatively by exciting phonons (②) or plasmons (③). The excited PPs either decay radiatively in terms of photons (④) or non-radiatively in terms of phonons (⑤). Therefore, two contributions are responsible for the emission of photoluminescence: radiative recombination through the electron–hole pair channel ① and radiative decay through the PP channel ④. The intensity ratio between two emission channels in the emission process is mainly determined by the d-hole scattering rate, which might be inversely proportional to the nanoparticle size. In consequence, the plasmons can be considered to play a twofold role during the whole Photoluminescence processes: in the excitation process they provide the local field enhancement, and in the emission process they offer extra radiation channels.

The above discussions on the emission mechanism of MPL is based on the fact that the lattice temperature is lower than the melting point of NPs, which could be referred to as in weak excitation case. In such a case, the NPs remain the designed sizes and shapes, the plasmonic nature plays an important role in the emission process of MPL. However, in the strong excitation situation, in which the lattice temperature is beyond the melting point, or the laser intensity is beyond the optical breakdown threshold, MPL shows distinct emission behaviors. For instance, the number of the absorbed photon for an optical
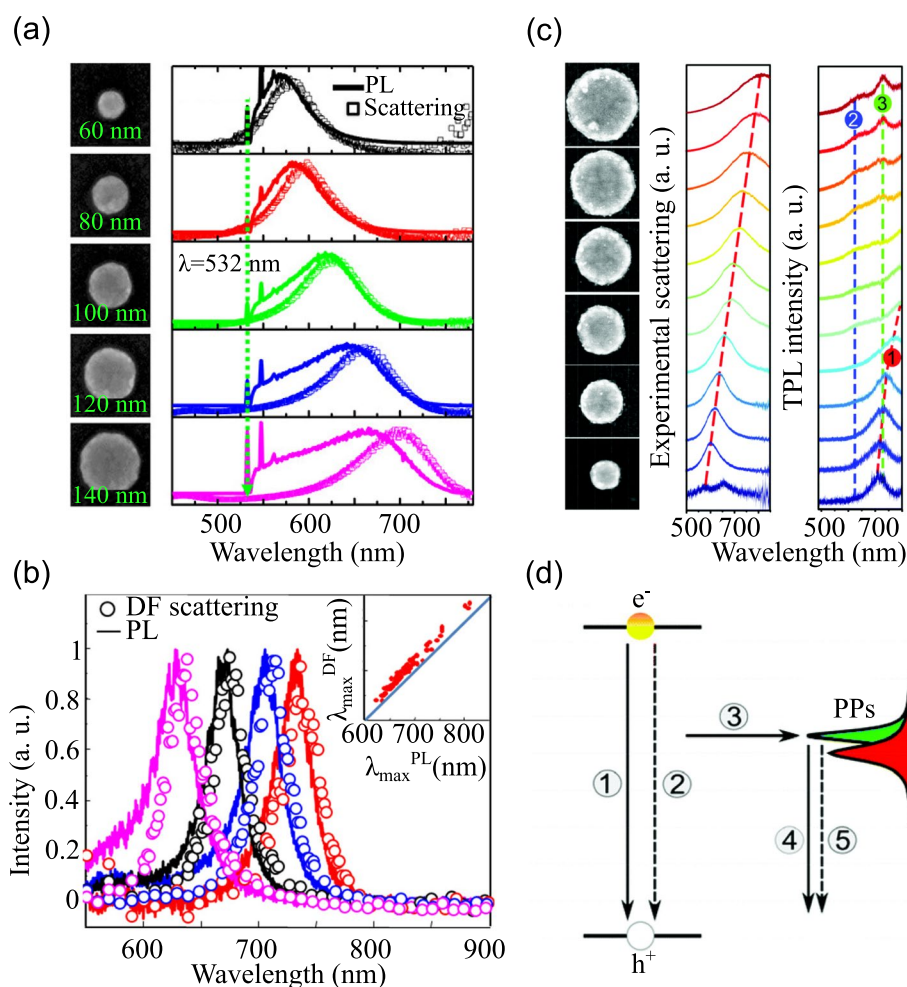
Fig. 10 Plasmonic fingerprints in the emission process of metallic photoluminescence. **a** Normalized OPL (solid line) and dark-field scattering (open squares) spectra of single gold discs. The disc diameter ranges from 60 to 140 nm with a step of 20 nm. Reprinted with permission from ACS Nano 2012, 6, 10,147–10155. Copyright 2012 American Chemical Society. **b** Normalized OPL (solid line) and dark-field scattering (open circles) spectra of single gold NRs. Inset: Relationship between the photoluminescence and scattering maxima. Reprinted with permission from ACS Nano 2012, 6(8), 7177–7184. Copyright 2012 American Chemical Society. **c** Normalized TPL and dark-field scattering spectra of single gold discs. The scale bar in the SEM images represents 100 nm. Three emission modes are visible in the TPL spectra: one mode whose peak position shifts to longer wavelengths as the disc size increases (mode 1) and two nearly stationary modes with a shoulder centered at 540 nm (mode 2, blue dashed line) and a sharper peak situated at around 630 nm (mode 3, green dashed line). Reprinted with permission from Nanoscale 2018, 10, 8240–8245. Copyright 2018 Royal Society of Chemistry. **d** Sketch for the physical mechanism of the photoluminescence emission. PPs represent particle plasmons. Reprinted with permission from Nanoscale 2018, 10, 8240–8245. Copyright 2018 Royal Society of Chemistry

transition, namely the power law exponent coefficient, is not larger than two in the weak excitations, due to the fast relaxation of the first excited electron in the conduction band [132]. Nevertheless, a value larger than 10 has been reported in the strong excitations, for example in the avalanche-like MPL (AMPL) from coupled gold nanowires, as shown in Fig. 11a [133, 134]. Similar phenomena were observed from Ag nanowire arrays and Au-Al nanodimers [135–137]. As shown in Fig. 11b, the power law exponent coefficient increases from 2 to 3 at certain critical incident laser intensity, which, however, don't
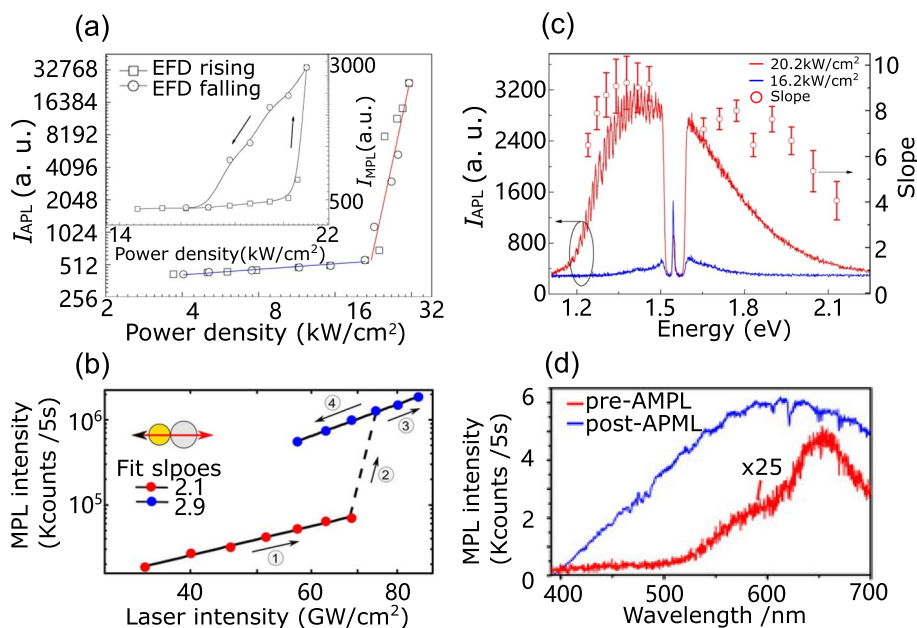
Fig. 11 Photoluminescence emission in the strong excitation case. **a** The excitation power dependence of integrated AMPL intensity appears as a typical bi-segmental curve in logarithm coordinate. AMPL threshold locates at around 20.2 kW/cm² and the two slopes are fitted to be b1 = 0.17 ± 0.02 and b2 = 10.87 ± 1.74, respectively. The inset shows a fine structure of the data curve around the threshold. Reprinted with permission from Scientific Reports 2016, 6, 18,857. Copyright 2016 Springer Nature Publishing Group. **b** Double logarithmic plot of the photoluminescence intensity from a single Au120–Al160 heterodimer as a function of the incident laser intensity. The incident beam is linearly polarized along the long dimer axis. Four regimes with different excitation intensity dependences are divided: ① pre-AMPL step, ② AMPL occurring step, ③ post-AMPL step with continuous increase in the incident intensity and ④ post-AMPL step with decreasing laser intensity. Reprinted with permission from The Journal of Chemical Physics 2021, 154, 074701. Copyright 2021 American Institute of Physics. **c** Photoluminescence spectra taken below (blue) and above (red) the AMPL threshold, respectively. Open circles with error bars represent the fitted slope values versus photon energy. Reprinted with permission from Scientific Reports 2016, 6, 18,857. Copyright 2016 Springer Nature Publishing Group. **d** MPL spectra of a single contacted Au120–Al160-g20 nanodimer before (red) and after (blue) the AMPL occurrence. For guiding the eyes, the emission signals of pre-AMPL are multiplied by 25. Reprinted with permission from The Journal of Chemical Physics 2021, 154, 074701. Copyright 2021 American Institute of Physics

recover to 2 even when the laser intensity decreases to the original value. Beside the emission intensity and the power law exponent coefficient, the emission spectra also show distinct profiles, such as linewidth broadening (Fig. 11c) and the loss of plasmonic footprints [137], as shown in Fig. 11d. The emission spectrum was regarded as surface plasmon assisted black body radiations in such a strong excitation case [134].

Advanced applications

SHG

Due to nonlinear dependences on the excitation laser intensity, nonlinear optical microscopy such as using SHG and two-photon fluorescence has intrinsic ability to restrict excitation to a tiny focal volume in the samples. Thus, a higher resolution can be obtained in comparison with the conventional optical microscope. Another advantage of nonlinear optical microscopy is a greater imaging depth, owing to reduced light scattering of long wavelengths that are used for excitation. Therefore, nonlinear optical signals

such as SHG and MPL open new perspectives towards the advanced applications for imaging in various scientific fields such as physics, chemistry and biology.

Hellwarth and Christensen first implemented an SHG based optical microscope to visualize the microscopic crystal structure in 1974 [138]. The first biological SHG image was reported by Freund in 1986 [139]. These images showed distinct contrast levels from regular (linear) microscopy. For instance, as shown in the left of Fig. 12a, Carvalho et. al. used a dark-field SHG microscope to efficiently probe grain boundaries and edges in monolayer dichalcogenides (i.e., $MoSe_2$, MoS_2, and WS_2) [140]. The frequency dependence of this emission in $MoSe_2$ monolayers was explained in terms of plasmon-enhanced SHG related to the defect's metallic character, as shown in the right of Fig. 12a. Due to a higher resolution in comparison with the linear emission microscopy, SHG is employed to detect the single NPs. As shown in Fig. 12b, Jin et. Al [65]. observed the single Ag monomers, dimers and nanorods by using the SH signals, which was confirmed by the transmission electron microscopy. The dependences of nanorods and dimers on the excitation polarization were explained using the one-photon resonant driven nonlinear oscillator response mechanism.

Besides of high-resolution imaging, since SHG is sensitive to the shape asymmetry of nanostructures, the far-field emission could reveal any small deviation (several nm) from slight size changes and perfectly symmetric shapes. Wang et. al. demonstrated that angle-resolved SHG was able to detect a diameter change with a resolution as high as 50 nm [15]. They used the linear polarized light but with varying polarization angles to excite the gold nanodimers and collected the far-field SHG intensity at each angle. The
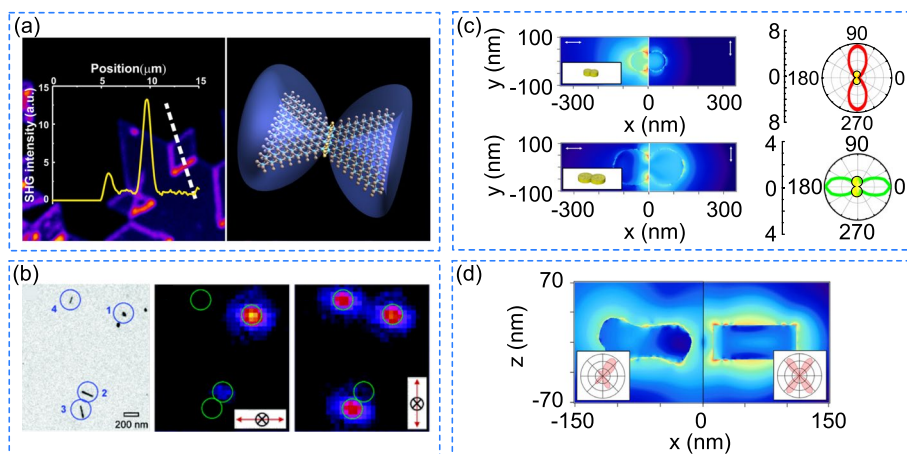
Fig. 12 SHG applications. (**a**) The grain boundaries and edges of the monolayer dichalcogenides were observed by using a dark-field SHG microscope. Reprinted with permission from Nano Letters 2020, 20, 284–291.

Copyright 2020 American Chemical Society. (**b**) Single silver nanodimer and nanorod were observed by using SHG mapping. Reprinted with permission from Journal of the American Chemical Society 2005, 127, 12,482–12,483. Copyright 2005 American Chemical Society. (**c**) Far-field SHG intensity plotted in a polar diagram showed a flip of 90° as the diameter of gold nanodimer increases. Reprinted with permission from The Journal of Physical Chemistry C 2016, 120, 17,699–17,710. Copyright 2016 American Chemical Society. (**d**) Far-field SHG intensity plotted in a polar diagram revealed a slight symmetry break in the shape of gold nanorod. Reprinted with permission from Nano Letters 2013, 13, 1787–1792. Copyright 2013 American Chemical Society

SHG polar maps from both the experiment and the calculation clearly showed a flip of 90° as the diameter increases, as shown in Fig. 12c. The reason they claimed was the switch of resonant plasmon mode. Jeremy et. al. found that a slight of surface roughness or deformation of a gold nanorod was clearly revealed by the angle-resolved far-field SHG, while linear responses barely handle, as shown in Fig. 12d [60]. They used a linear polarized light which was along the long axis of nanorod, and calculated the angle-resolved SHG intensity in the detection path. Further studies show that angle-resolved far-field SHG keeps their sensitivities to the geometric change in the excitation optical path as well. These investigations unambiguously evidence that SHG is a promising tool for sensitive optical characterizations of plasmonic nanostructures and for the advanced applications in sensing the displacement, the temperature, the pressure, the thermal deformation and so on.

MPL

We now turn our attentions to the applications of MPL. We show some examples from the aspects of TPA, relaxation and emission stages of a MPL process sequentially.

As we analyzed in session 3.4, one of the key roles of PPs in a MPL process is to provide strong electromagnetic field enhancement in the excitation stage, i.e., TPA. This usually can be realized by matching the LSPR of nanoantennas to the fundamental laser wavelength. The plasmon enhanced TPA process leads to numerous applications, involving entangled TPA [141], high-performance silicon-based optical correlators [142] and medical thermal therapies [143]. As shown in Fig. 13a1, Smoleaninov A et. al. designed and fabricated a coaxial split-ring and disc array to enhance the photocurrent of a Si photodiode [142]. They compared the responsivity of the photodetector with and without nanoantennas in different collection wavelengths, as shown in Fig. 13a2 ~ a4. They observed that the nanoantenna array on the photodetector surface increased the TPA-induced peak photocurrent generation by factors of 2.77, 2.97 and 3.07 at the wavelengths of 1340, 1400 and 1550 nm, respectively [142]. This kind of photodiode can generally overcome the limit of material bandgaps and provide a considerably broad-band detection. In addition, by taking the full advantages of thermal energy associated with TPA process, noble metal NPs become ideal nanoscale heat sources for the treatment of photodynamic therapy and photothermal therapy [143–145]. For example, Kong et al. designed and constructed a metal-fluorophore microhybrid combining silver NPs and cyano-carboxylic carbazole derivative (Ag-CECZA) [143]. The TPA cross-section of Ag-CECZA was found 13 times higher than that of pure CECZA. After the injection into the Hela cells and irradiated with a 780-nm continuous-wavelength laser, almost 54% of the Hela cells were killed, which demonstrated the high photothermal conversion efficiency of such plasmonic-enhanced metal-fluorophore complex.

As a special case of linear and nonlinear optical absorption, saturation absorption (SA) becomes an indispensable process for the material-based SAs, in order to achieve a stable passive mode-locking for the ultrafast lasers. Colloidal nanorods were firstly proposed to serve as plasmonic-assisted SAs [146–148]. However, the optical properties of such colloids behave more like averaged ones due to dispersed sizes and random orientation, and in the end the conclusions drawn have been poorly linked to the plasmonic nature. Wang et al., however, employed planar nanotechnologies to fabricate 2D
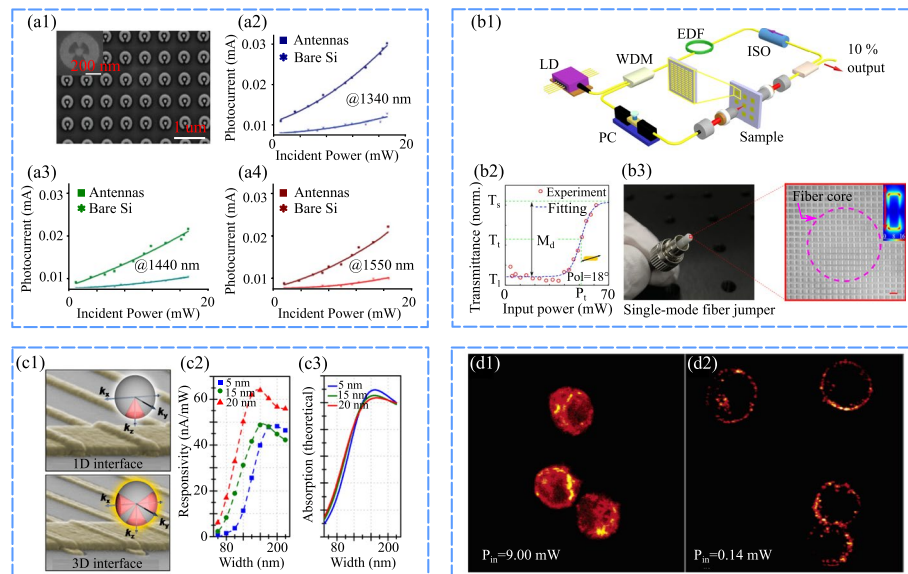
Fig. 13 MPL applications. **a** A plasmonic split-ring and disc array were fabricated to enhance the photocurrent of a Si photodiode: (a1) The SEM images of the plasmonic nanoantennas; (a2 ~ a4) Photocurrent comparisons between the photodiodes with the antennas and the ones without antennas in different collection wavelengths. Reprinted with permission from Optics Letters 2016, 41(19), 4445–4448. Copyright 2016 Optical Society of American. **b** Plasmonic metasurfaces served as SAs in the fiber laser cavities: (b1) Plasmonic metasurface SA were implemented into a free space-coupled fiber laser cavity; (b2) Nonlinear transmission spectrum of the gold nanorod metasurface; (b3) The gold nanorod metasurfaces were fabricated on the endface of a commercial single-mode fiber jumper. Reprinted with permission from Light: Science & Applications 2020, 9, 50 (b1,b2) and Light: Advanced Manufacturing 2022, 3, 45 (b3). Copyright 2020 Springer Nature Publishing Group and 2022 Jihua Laboratory. **c** Plasmon enhanced Schottky photodetectors: (c1) Schematic images of the 1D and 3D plasmonic Schottky photodetector; (c2) Experimental photocurrent responsivity and theoretical calculation of absorption at $\lambda = 1500$ nm for embedding depths of 5 nm (blue), 15 nm (green), and 25 nm (red). Reprinted with permission from Nano Letters 2013, 13, 1687 − 1692. Copyright 2013 American Chemical Society. **d** Two-photon images of cancer cells: (d1) Two-photon autofluorescence image of unlabeled cells; (d2) TPL image of nanorod-labeled cells. Reprinted with permission from Nano Letters 2007, 7, 941–945. Copyright 2007 American Chemical Society

plasmonic metasurfaces and integrated them within a free-space coupled fiber laser architecture, as illustrated in Fig. 13b1 [63]. They finally obtained a stable self-starting mode-locked laser operation with a typical single soliton pulse duration of 729 fs, and a large signal-to-noise ratio of 75 dB in the radio-frequency domain [63]. Remarkably, matching the fundamental frequency to the longitudinal dipolar plasmon mode, they measured the modulation depth of the saturable absorption of such plasmonic metasurfaces as high as 60%, as shown in Fig. 13b2. More recently, the same research group further integrated the well-defined plasmonic metasurfaces on the endfaces of commercial single mode fiber jumpers, and implemented so called metafiber into an all-fiber laser cavity, as illustrated in Fig. 13b3 [64]. By tuning the plasmonic resonances to different optical wavelengths, they finally achieved all-fiber sub-picosecond (minimum 513 fs) soliton mode locked lasers at 1.5 μm and 2 μm wavebands. The work opened a virgin towards ultrathin nonlinear plasmonic devices for the applications where tunable nonlinear transfer functions are needed, such as in ultrafast lasers, optical frequency combs or neuromorphic circuits.

Relying on the ultrafast relaxation time of hot carriers in the process of MPL, a variety of devices including broad-band solar cells [149, 150], complementary

metal–oxide–semiconductor compatible on-chip sensors [151, 152] and ultrasensitive near-infrared photodetectors [153, 154] were intensively studied. A common way to enhance the responsivity and work wavebands for the photodetectors is to combine a metallic nanostructure with a semiconductor, forming the well-known Schottky barrier. In such configurations, the hot electrons from the plasmon decay can contribute to the semiconductor photocurrent even for the excitation energies below the bandgap of the semiconductor. In 2011, Knight et al. fabricated the gold nanorods on the surface of a n-type Si photodiode [153]. They found that the photocurrent follows similar profiles of the absorption spectra of individual nanorods, demonstrating that the photocurrents generated from the Schottky photodiode were indeed tailored by the plasmon resonances. In one of their following works, they changed the nanorods array into gold nanowires to better couple the incident light [154]. They found that the embedded depth and the width significantly alter the responsivity of the Schottky photodetector, as seen in Fig. 13c1-c2, which were shaped by the plasmonic absorptions of nanowires. These facts confirm that the photocurrents are indeed from the hot electrons decayed from the plasmon energy levels.

Using metallic NPs as contrast agents to image the tissues or even the single cells in situ have attracted much interest for the biologists in the past two decades [155–158]. TPL and three-photon luminescence are among the most investigated nonlinear optical responses for the applications in biological imaging thanks to their relatively large penetration depths and the efficient quantum yield enhanced by the surface plasmons [156]. For example, by tuning the longitudinal dipolar resonances of gold nanorods to the near-infrared regime, Durr et al. found that the TPL intensity from gold-nanorod-labeled cancer cells was 3 orders of magnitude brighter than the two-photon autofluorescence emission intensity from unlabeled cancer cells [159]. This would allow a sufficiently high resolution and penetration depth of the bioimaging at a relatively low excitation laser power and thus prevent the live cells from thermal damages. As it was shown in Fig. 13d1, d2, the imaging required 9 mW of excitation power in unlabeled cells to get same signal level obtained with mere 0.14 mW for nanorod labeled cells [159]. Their strong signal, resistance to photobleaching, ease of synthesis and biocompatibility make gold nanorods an attractive contrast agent for two-photon imaging.

Conclusion and outlooks

As one of the most significant components in plasmonics, its nonlinear effects like SHG and MPL have aroused intensive interest in the past decades. This review provides in-depth physical insights into the light-matter interactions in such a nonlinear regime, and reveals the fundamental rules and potential applications for SHG and MPL, casting the light on the related theoretical modeling as well as experimental demonstrations. In particular, we systematically analyze the key factors giving rise to a strongly plasmon-enhanced SHG radiation and each physical step of a MPL process. We further highlight their potential applications in ultra-sensitive sensors or detectors, super-resolution imaging, efficient photon harvesting and other ultra-compact electro-optic/optoelectronic devices.

By patterning the plasmonic nanoparticles in 2D arrays, nonlinear metasurfaces are under intense investigations in recent years to manipulate structured light fields with

complex spatial distributions, tailored phase profiles, customized polarization states and quantum angular momentums [160–166]. The nonlinear plasmonic effects such as SHG and MPL provide a foundation for the design and implementation of nonlinear metasurfaces. They enable enhanced nonlinear signal generation, localized field engineering, nonlinear wavefront manipulation, and tunable nonlinear responses. These fundamental roles drive the development of nonlinear metasurfaces with advanced applications in optical communication [167, 168], imaging [169], holography, and optical trapping [170, 171], As shown in Fig. 14.

Nevertheless, as the conversion yields of nonlinear optical processes are generally low, which require a much higher fundamental intensity than linear optical responses, undesirable thermal damages become one of the key challenges for the nonlinear plasmonic devices, hampering their wide adoptions in practical usages. This particularly holds for the noble metal nanostructures, as their melting points are relatively low, e. g. around 1000 K for gold [123]. To circumvent this problem, a straightforward solution could be encapsulating the plasmonic nanostructures with a protection layer which has a much higher melting point. The protection material could be for example silica glass or transparent ceramics compatible with current nanofabrication technologies. It is noteworthy that even the shape of nanostructures could be well preserved, the plasmonic properties, e. g. the resonance peak position and linewidth, would still undergo slight variances due to a significant lattice temperature change [172]. Another way to circumvent the thermal damage issue is to use alternative plasmonic materials. Such kinds of materials own either a relative high melting point than the commonly used noble metals or their nonlinear properties can be triggered by other factors, such as electro-optic effect and acousto-optic effect. TiN is among the most investigated candidates from the former respect due to a similar dispersion relation to gold but three times higher the melting point [173]. The high melting point, strong insulations to the harsh environment and good biocompatibility allow TiN to apply in multiple fields, including broadband absorbers,
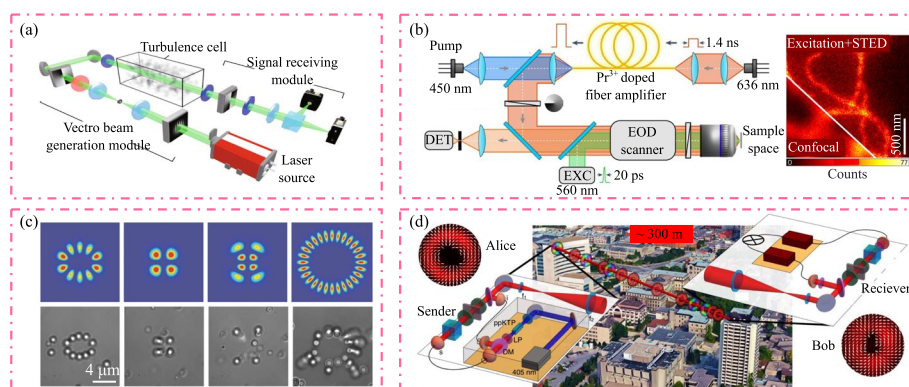
Fig. 14 Promising applications of structured light fields. **a** Vector light was used in optical communications through strongly scattered medium. Reprinted with permission from Nature communications, 2021, 12 (1): 1666. Copyright 2021 Springer Nature Publishing Group. **b** Donut-mode light was used in super-resolution optical microscope. Reprinted with permission from Nature Biotechnology 2022, 22, 01519. Copyright 2022 Springer Nature Publishing Group. **c** The structured light was used in optical trapping. Reprinted with permission from Applied physics letters, 2011, 98(11). Copyright 2011 AIP Publishing Group. **d** The vortex light was used in quantum encryption. Reprinted with permission from Optica 2017, 4, 1006–1010. Copyright 2017 Optical Society of American

nonlinear optic crystals, protective or decorative coatings as well as photoacoustic and photothermal agents [173–175]. From the latter aspect, the nonlinear polymers could be the most promising candidates to lower down the fundamental laser intensities, as their third-order susceptibilities could be easily tuned by using bias voltages, instead of relying on the light-induced nonlinearities [176–178]. State-of-art nanofabrication technologies have successfully manipulated the metallic polymers into well-defined nanoscale patterns, demonstrating their applications in electrically beam-steering switcher [178]. This opens a new avenue for the integration and miniaturization of the plasmonic or metasurfaces devices, both in linear and nonlinear regimes.

Availability of data and materials
Data sharing is not applicable to this article as no new datasets were created in this review.

Declarations

Ethics approval and consent to participate
Not applicable.

Consent for publication
Not applicable.

Competing interests
The authors declare no competing financial interests.

References
1. Boyd RW. Nonlinear optics. New York: Academic Press; 2008.
2. Maiman TH. Stimulated optical radiation in ruby. Nature. 1960;187:493–4. https://doi.org/10.1038/187493a0.
3. Butet J, et al. Optical second harmonic generation in plasmonic nanostructures: from fundamental principles to advanced applications. ACS Nano. 2015;9:10545–62. https://doi.org/10.1021/acsnano.5b04373.
4. Porto JA, et al. Optical bistability in subwavelength slit apertures containing nonlinear media. Phys Rev B. 2004;70:81402. https://doi.org/10.1103/PhysRevB.70.081402.
5. Ricard D, et al. Surface-mediated enhancement of optical phase conjugation in metal colloids. Opt Lett. 1985;10:511–3. https://doi.org/10.1364/ol.10.000511.
6. Chen PY, Alu A. Subwavelength imaging using phase-conjugating nonlinear nanoantenna arrays. Nano Lett. 2011;11:5514–8. https://doi.org/10.1021/nl203354b.
7. Slusher RE, et al. Observation of squeezed states generated by four-wave mixing in an optical cavity. Phys Rev Lett. 1985;55:2409–12. https://doi.org/10.1103/PhysRevLett.55.2409.
8. Deng L, et al. Four-wave mixing with matter waves. Nature. 1999;398:218–20. https://doi.org/10.1038/18395.
9. Malkin VM, et al. Detuned raman amplification of short laser pulses in plasma. Phys Rev Lett. 2000;84:1208–11. https://doi.org/10.1103/PhysRevLett.84.1208.
10. Liang TK, Tsang HK. Role of free carriers from two-photon absorption in Raman amplification in silicon-on-insulator waveguides. Appl Phys Lett. 2004;84:2745–7. https://doi.org/10.1063/1.1702133.
11. Cheng W, et al. Reaching the nonlinear regime of Raman amplification of ultrashort laser pulses. Phys Rev Lett. 2005;94:045003. https://doi.org/10.1103/PhysRevLett.94.045003.
12. Chiao RY, et al. Stimulated Brillouin scattering and coherent generation of intense hypersonic waves. Phys Rev Lett. 1964;12:592–5. https://doi.org/10.1103/PhysRevLett.12.592.
13. Zhu Z, et al. Stored light in an optical fiber via stimulated Brillouin scattering. Science. 2007;318:1748–50. https://doi.org/10.1126/science.1149066.
14. Farrer RA, et al. Highly efficient multiphoton-absorption-induced luminescence from gold nanoparticles. Nano Lett. 2005;5:1139–42. https://doi.org/10.1021/nl050687r.

15. Wang J, et al. Direct comparison of second harmonic generation and two-photon photoluminescence from single connected gold nanodimers. J Phys Chem C. 2016;120:17699–710. https://doi.org/10.1021/acs.jpcc.6b04850.

16. Eberly JH, et al. Nonlinear light scattering accompanying multiphoton ionization. Phys Rev Lett. 1989;62:881–4. https://doi.org/10.1103/PhysRevLett.62.881.

17. Corkum PB. Plasma perspective on strong field multiphoton ionization. Phys Rev Lett. 1993;71:1994–7. https://doi.org/10.1103/PhysRevLett.71.1994.

18. Popov VS. Tunnel and multiphoton ionization of atoms and ions in a strong laser field (Keldysh theory). Phys Usp. 2004;47:855–85. https://doi.org/10.1070/PU2004v047n09ABEH001812.

19. Wang J, et al. Strong second-harmonic generation from Au-Al heterodimers. Nanoscale. 2019;11:23475–81. https://doi.org/10.1039/c9nr07644a.

20. Agrawal GP. Nonlinear fiber optics. New York: Acedemic Press; 2010.

21. Friberg S, Smith P. Nonlinear optical glasses for ultrafast optical switches. IEEE J Quantum Electron. 1987;23:2089–94. https://doi.org/10.1109/jqe.1987.1073278.

22. Heebner JE, Boyd RW. Enhanced all-optical switching by use of a nonlinear fiber ring resonator. Opt Lett. 1999;24:847–9. https://doi.org/10.1364/ol.24.000847.

23. Russell P. Photonic crystal fibers. Science. 2003;299:358–62. https://doi.org/10.1126/science.1079280.

24. Krauss TF. Slow light in photonic crystal waveguides. J Phys D Appl Phys. 2007;40:2666–70. https://doi.org/10.1088/0022-3727/40/9/s07.

25. Dudley JM, Taylor JR. Supercontinuum generation in optical fibers. New York: Cambridge University Press; 2010.

26. Alfano RR, Shapiro SL. Observation of self-phase modulation and small-scale filaments in crystals and glasses. Phys Rev Lett. 1970;24:592–4. https://doi.org/10.1103/PhysRevLett.24.592.

27. Maier SA. Plasmonics: fundamentals and applications. New York: Springer; 2007.

28. de Aberasturi DJ, et al. Modern applications of plasmonic nanoparticles: from energy to health. Adv Opt Mat. 2015;3:602–17. https://doi.org/10.1002/adom.201500053.

29. Ding S-Y, et al. Nanostructure-based plasmon-enhanced Raman spectroscopy for surface analysis of materials. Nat Rev Mater. 2016;1:6. https://doi.org/10.1038/natrevmats.2016.21.

30. Li JF, et al. Plasmon-enhanced fluorescence spectroscopy. Chem Soc Rev. 2017;46:3962–79. https://doi.org/10.1039/c7cs00169j.

31. Jaculbia RB, et al. Single-molecule resonance Raman effect in a plasmonic nanocavity. Nat Nanotechnol. 2020;15:105–10. https://doi.org/10.1038/s41565-019-0614-8.

32. Cong B, et al. Gold nanorods: near-infrared plasmonic photothermal conversion and surface coating. J Mat Sci Chem Engine. 2014;2:20–5. https://doi.org/10.4236/msce.2014.21004.

33. Furube A, Hashimoto S. Insight into plasmonic hot-electron transfer and plasmon molecular drive: new dimensions in energy conversion and nanofabrication. NPG Asia Mat. 2017;9:e454–e454. https://doi.org/10.1038/am.2017.191.

34. Mallah AR, et al. Plasmonic nanofluids for high photothermal conversion efficiency in direct absorption solar collectors: Fundamentals and applications. Solar Energy Mat Solar Cells. 2019;201:110084. https://doi.org/10.1016/j.solmat.2019.110084.

35. Mooradian A. Photoluminescence of metals. Phys Rev Lett. 1969;22:185–7. https://doi.org/10.1103/PhysRevLett.22.185.

36. Boyd GT, et al. Photoinduced luminescence from the noble metals and its enhancement on roughened surfaces. Phys Rev B: Condens Matter. 1986;33:7923–36. https://doi.org/10.1103/physrevb.33.7923.

37. Wang J, et al. Carrier recombination and plasmonic emission channels in metallic photoluminescence. Nanoscale. 2018;10:8240–5. https://doi.org/10.1039/c7nr07821h.

38. Bohren CF, Huffman DR. Absorption and scattering of light by small particles. New York: Wiley; 1998.

39. Nehl CL, et al. Scattering spectra of single gold nanoshells. Nano Lett. 2004;4:2355–9. https://doi.org/10.1021/nl048610a.

40. Wen F, et al. Charge transfer plasmons: optical frequency conductances and tunable infrared resonances. ACS Nano. 2015;9:6428–35. https://doi.org/10.1021/acsnano.5b02087.

41. Cho EC, et al. Measuring the optical absorption cross-sections of Au-Ag nanocages and Au nanorods by photoacoustic imaging. J Phys Chem C. 2009;113:9023–8. https://doi.org/10.1021/jp903343p.

42. Zhang N, et al. Near-field dielectric scattering promotes optical absorption by platinum nanoparticles. Nat Photonics. 2016;10:473–82. https://doi.org/10.1038/nphoton.2016.76.

43. Wackenhut F, et al. Multicolor microscopy and spectroscopy reveals the physics of the one-photon luminescence in gold nanorods. J Phys Chem C. 2013;117:17870–7. https://doi.org/10.1021/jp407353r.

44. Bouhelier A, et al. Near-field second-harmonic generation induced by local field enhancement. Phys Rev Lett. 2003;90:013903. https://doi.org/10.1103/PhysRevLett.90.013903.

45. Dong Z, et al. Second-harmonic generation from sub-5 nm gaps by directed self-assembly of nanoparticles onto template-stripped gold substrates. Nano Lett. 2015;15:5976–81. https://doi.org/10.1021/acs.nanolett.5b02109.

46. Wang Z, et al. Selectively plasmon-enhanced second-harmonic generation from monolayer tungsten diselenide on flexible substrates. ACS Nano. 2018;12:1859–67. https://doi.org/10.1021/acsnano.7b08682.

47. Kruk SS, et al. Asymmetric parametric generation of images with nonlinear dielectric metasurfaces. Nat Photonics. 2022;16:561–5. https://doi.org/10.1038/s41566-022-01018-7.

48. Stockman MI, et al. Enhanced second-harmonic generation by metal surfaces with nanoscale roughness: nanoscale dephasing, depolarization, and correlations. Phys Rev Lett. 2004;92:057402. https://doi.org/10.1103/PhysRevLett.92.057402.

49. Bachelier G, et al. Origin of optical second-harmonic generation in spherical gold nanoparticles: Local surface and nonlocal bulk contributions. Phys Rev B. 2010;82:235403. https://doi.org/10.1103/PhysRevB.82.235403.

50. Butet J, et al. Optical second harmonic generation of single metallic nanoparticlesembedded in a homogeneous medium. Nano Lett. 2010;10:1717–21. https://doi.org/10.1021/nl1000949.

51. Zhang, et al. Three-dimensional nanostructures as highly efficient generators of second harmonic light. Nano Lett. 2011;11:5519–23. https://doi.org/10.1021/nl2033602.

52. Butet J, et al. Surface second-harmonic generation from coupled spherical plasmonic nanoparticles: eigenmode analysis and symmetry properties. Phys Rev B. 2014;89:245449. https://doi.org/10.1103/PhysRevB.89.245449.

53. Zhang T, et al. Coherent second harmonic generation enhanced by coherent plasmon-exciton coupling in plasmonic nanocavities. ACS Photonics. 2023;10:1529–37. https://doi.org/10.1021/acsphotonics.3c00105.

54. Hentschel M, et al. Quantitative modeling of the third harmonic emission spectrum of plasmonic nanoantennas. Nano Lett. 2012;12:3778–82. https://doi.org/10.1021/nl301686x.

55. Navarro-Cia M, Maier SA. Broad-band near-infrared plasmonic nanoantennas for higher harmonic generation. ACS Nano. 2012;6:3537–44. https://doi.org/10.1021/nn300565x.

56. Hajisalem G, et al. Probing the quantum tunneling limit of plasmonic enhancement by third harmonic generation. Nano Lett. 2014;14:6651–4. https://doi.org/10.1021/nl503324g.

57. Danckwerts M, Novotny L. Optical frequency mixing at coupled gold nanoparticles. Phys Rev Lett. 2007;98:026104. https://doi.org/10.1103/PhysRevLett.98.026104.

58. Biagioni P, et al. Dynamics of four-photon photoluminescence in gold nanoantennas. Nano Lett. 2012;12:2941–7. https://doi.org/10.1021/nl300616s.

59. Xu J, et al. Multiphoton upconversion enhanced by deep subwavelength near-field confinement. Nano Lett. 2021;21:3044–51. https://doi.org/10.1021/acs.nanolett.1c00232.

60. Butet J, et al. Ultrasensitive optical shape characterization of gold nanoantennas using second harmonic generation. Nano Lett. 2013;13:1787–92. https://doi.org/10.1021/nl400393e.

61. Galanty M, et al. Second harmonic generation hotspot on a centrosymmetric smooth silver surface. Light Sci Appl. 2018;7:49. https://doi.org/10.1038/s41377-018-0053-6.

62. Berini P. Surface plasmon photodetectors and their applications. Laser Photonics Rev. 2014;8:197–220. https://doi.org/10.1002/lpor.201300019.

63. Wang J, et al. Saturable plasmonic metasurfaces for laser mode locking. Light Sci Appl. 2020;9:50. https://doi.org/10.1038/s41377-020-0291-2.

64. Zhang L, et al. Plug-and-play'plasmonic metafibers for ultrafast fibre lasers. Light Adv Manufact. 2022;3:45. https://doi.org/10.37188/lam.2022.045.

65. Jin R, et al. Correlating second harmonic optical responses of single Ag nanoparticles with morphology. J Am Chem Soc. 2005;127:12482–3. https://doi.org/10.1021/ja0537169.

66. Butet J, et al. Three-dimensional mapping of single gold nanoparticles embedded in a homogeneous transparent matrix using optical second-harmonic generation. Opt Express. 2010;18:22314–23. https://doi.org/10.1364/OE.18.022314.

67. Accanto N, et al. Phase control of femtosecond pulses on the nanoscale using second harmonic nanoparticles. Light Sci Appl. 2014;3:e143–e143. https://doi.org/10.1038/lsa.2014.24.

68. Accanto N, et al. Capturing the optical phase response of nanoantennas by coherent second-harmonic microscopy. Nano Lett. 2014;14:4078–82. https://doi.org/10.1021/nl501588r.

69. Nuriya M, et al. Multimodal two-photon imaging using a second harmonic generation-specific dye. Nat Commun. 2016;7:11557. https://doi.org/10.1038/ncomms11557.

70. Zipfel WR, et al. Nonlinear magic: multiphoton microscopy in the biosciences. Nat Biotechnol. 2003;21:1369–77. https://doi.org/10.1038/nbt899.

71. Lakowicz JR, et al. Plasmon-controlled fluorescence: a new paradigm in fluorescence spectroscopy. Analyst. 2008;133:1308–46. https://doi.org/10.1039/b802918k.

72. Kauranen M, Zayats AV. Nonlinear plasmonics. Nat Photonics. 2012;6:737–48. https://doi.org/10.1038/nphoton.2012.244.

73. Metzger B, et al. Ultrafast nonlinear plasmonic spectroscopy: from dipole nanoantennas to complex hybrid plasmonic structures. ACS Photonics. 2016;3:1336–50. https://doi.org/10.1021/acsphotonics.5b00587.

74. Butet J, Martin OJ. Nonlinear plasmonic nanorulers. ACS Nano. 2014;8:4931–9. https://doi.org/10.1021/nn500943t.

75. Yang ZJ, et al. Efficient second harmonic generation in gold-silicon core-shell nanostructures. Opt Express. 2018;26:5835–44. https://doi.org/10.1364/OE.26.005835.

76. Ding SJ, et al. Magnetic plasmon-enhanced second-harmonic generation on colloidal gold nanocups. Nano Lett. 2019;19:2005–11. https://doi.org/10.1021/acs.nanolett.9b00020.

77. Hou J, et al. Self-induced transparency in a perfectly absorbing chiral second-harmonic generator. PhotoniX. 2022;3:22. https://doi.org/10.1186/s43074-022-00068-y.

78. Loudon R. The quantum theory of light. New York: Oxford University Press; 2000.

79. Shen YR. The principles of nonlinear optics. New York: Wiley; 1984.

80. Simon HJ, et al. Optical second-harmonic generation with surface plasmons in silver films. Phys Rev Lett. 1974;33:1531–4. https://doi.org/10.1103/PhysRevLett.33.1531.

81. Shan J, et al. Experimental study of optical second-harmonic scattering from spherical nanoparticles. Phys Rev A. 2006;73:023819. https://doi.org/10.1103/PhysRevA.73.023819.

82. Dadap JI. Optical second-harmonic scattering from cylindrical particles. Phys Rev B. 2008;78:205322. https://doi.org/10.1103/PhysRevB.78.205322.

83. Bloembergen N, et al. Optical second-harmonic generation in reflection from media with inversion symmetry. Phys Rev. 1968;174:813–22. https://doi.org/10.1103/PhysRev.174.813.

84. O'Brien K, et al. Predicting nonlinear properties of metamaterials from the linear response. Nat Mater. 2015;14:379–83. https://doi.org/10.1038/nmat4214.

85. Celebrano M, et al. Mode matching in multiresonant plasmonic nanoantennas for enhanced second harmonic generation. Nature Nanotechnol. 2015;10:412–7. https://doi.org/10.1038/nnano.2015.69.

86. Linnenbank H, Linden S. Second harmonic generation spectroscopy on second harmonic resonant plasmonic metamaterials. Optica. 2015;2:698–701. https://doi.org/10.1364/optica.2.000698.

87. Metzger B, et al. Third-harmonic spectroscopy and modeling of the nonlinear response of plasmonic nanoantennas. Opt Lett. 2012;37:4741–3. https://doi.org/10.1364/ol.37.004741.

88. Demtroder W. Laser spectroscopy: basic concepts and instrumentation. New York: Springer; 2003.

89. Pu Y, et al. Nonlinear optical properties of core-shell nanocavities for enhanced second-harmonic generation. Phys Rev Lett. 2010;104:207402. https://doi.org/10.1103/PhysRevLett.104.207402.

90. Chen S, et al. Strong nonlinear optical activity induced by lattice surface modes on plasmonic metasurface. Nano Lett. 2019;19:6278–83. https://doi.org/10.1021/acs.nanolett.9b02417.

91. Hooper DC, et al. Second harmonic spectroscopy of surface lattice resonances. Nano Lett. 2019;19:165–72. https://doi.org/10.1021/acs.nanolett.8b03574.

92. Shen B, et al. Nonlinear spectral-imaging study of second- and third-harmonic enhancements by surface-lattice resonances. Adv Opt Mat. 2020;8:1901981. https://doi.org/10.1002/adom.201901981.

93. Spackova B, Homola J. Sensing properties of lattice resonances of 2D metal nanoparticle arrays: an analytical model. Opt Express. 2013;21:27490–502. https://doi.org/10.1364/oe.21.027490.

94. Smith EM, et al. Second harmonic generation enhancement of ITO-based ENZ materials and metasurfaces. MRS Adv. 2022;7:741–5. https://doi.org/10.1557/s43580-022-00353-9.

95. Argyropoulos C, et al. Giant second-harmonic generation efficiency and ideal phase matching with a double ε-near-zero cross-slit metamaterial. Phys Rev B. 2014;89:235401. https://doi.org/10.1103/PhysRevB.89.235401.

96. Deng J, et al. Giant enhancement of second-order nonlinearity of epsilon-near- zero medium by a plasmonic metasurface. Nano Lett. 2020;20:5421–7. https://doi.org/10.1021/acs.nanolett.0c01810.

97. Metzger B, et al. Strong enhancement of second harmonic emission by plasmonic resonances at the second harmonic wavelength. Nano Lett. 2015;15:3917–22. https://doi.org/10.1021/acs.nanolett.5b00747.

98. Thyagarajan K, et al. Enhanced second-harmonic generation from double resonant plasmonic antennae. Opt Express. 2012;20:12860–5. https://doi.org/10.1364/OE.20.012860.

99. Ren ML, et al. Giant enhancement of second harmonic generation by engineering double plasmonic resonances at nanoscale. Opt Express. 2014;22:28653–61. https://doi.org/10.1364/OE.22.028653.

100. Guo K, Guo Z. Enhanced second-harmonic generation from Fano like resonance in an asymmetric homodimer of gold elliptical nanodisks. ACS Omega. 2019;4:1757–62. https://doi.org/10.1021/acsomega.8b02986.

101. Chandrasekar R, et al. Second harmonic generation with plasmonic metasurfaces: direct comparison of electric and magnetic resonances. Opt Mat Expr. 2015;5:2682–91. https://doi.org/10.1364/ome.5.002682.

102. Linden S, et al. Collective effects in second-harmonic generation from split-ring-resonator arrays. Phys Rev Lett. 2012;109:015502. https://doi.org/10.1103/PhysRevLett.109.015502.

103. Tsai WY, et al. Second Harmonic Light Manipulation with Vertical Split Ring Resonators. Adv Mat. 2019;31:1806479. https://doi.org/10.1002/adma.201806479.

104. Valev VK, et al. Plasmonic ratchet wheels: switching circular dichroism by arranging chiral nanostructures. Nano Lett. 2009;9:3945–8. https://doi.org/10.1021/nl9021623.

105. Valev VK, et al. Plasmons reveal the direction of magnetization in nickel nanostructures. ACS Nano. 2011;5:91–6. https://doi.org/10.1021/nn102852b.

106. Husu H, et al. Metamaterials with tailored nonlinear optical response. Nano Lett. 2012;12:673–7. https://doi.org/10.1021/nl203524k.

107. Canfield BK, et al. Local field asymmetry drives second-harmonic generation in non-centrosymmetric nanodimers. Nano Lett. 2007;7:1251–5. https://doi.org/10.1021/nl0701253.

108. Xu T, et al. Second-harmonic emission from sub-wavelength apertures: effects of aperture symmetry and lattice arrangement. Opt Express. 2007;15:13894–906. https://doi.org/10.1364/oe.15.013894.

109. Schon P, et al. Enhanced second-harmonic generation from individual metallic nanoapertures. Opt Lett. 2010;35:4063–5. https://doi.org/10.1364/OL.35.004063.

110. Berthelot J, et al. Silencing and enhancement of second-harmonic generation in optical gap antennas. Opt Express. 2012;20:10498–508. https://doi.org/10.1364/OE.20.010498.

111. Viarbitskaya S, et al. Delocalization of nonlinear optical responses in plasmonic nanoantennas. Phys Rev Lett. 2015;115:197401. https://doi.org/10.1103/PhysRevLett.115.197401.

112. Grosse NB, et al. Nonlinear plasmon-photon interaction resolved by k-space spectroscopy. Phys Rev Lett. 2012;108:136802. https://doi.org/10.1103/PhysRevLett.108.136802.

113. Li Y, et al. Transversely divergent second harmonic generation by surface plasmon polaritons on single metallic nanowires. Nano Lett. 2017;17:7803–8. https://doi.org/10.1021/acs.nanolett.7b04016.

114. Imura K, et al. Near-field two-photon-induced photoluminescence from single gold nanorods and imaging of plasmon modes. J Phys Chem B. 2005;109:13214–20. https://doi.org/10.1021/jp051631o.

115. Rosei R, Lynch DW. Thermomodulation spectra of Al, Au, and Cu. Phys Rev B. 1972;5:3883–94. https://doi.org/10.1103/PhysRevB.5.3883.

116. Rosei R, et al. d bands position and width in gold from very low temperature thermomodulation measurements. Surf Sci. 1973;37:689–99. https://doi.org/10.1016/0039-6028(73)90359-2.

117. Rosei R, et al. Temperature modulation of the optical transitions involving the Fermi surface in Ag: experimental. Phys Rev B. 1974;10:484–9. https://doi.org/10.1103/PhysRevB.10.484.

118. Guerrisi M, et al. Splitting of the interband absorption edge in Au. Phys Rev B. 1975;12:557–63. https://doi.org/10.1103/PhysRevB.12.557.

119. Hohlfeld J, et al. Electron and lattice dynamics following optical excitation of metals. Chem Phys. 2000;251:237–58. https://doi.org/10.1016/s0301-0104(99)00330-4.

120. Hu H, et al. Plasmon-modulated photoluminescence of individual gold nanostructures. ACS Nano. 2012;6:10147–55. https://doi.org/10.1021/nn3039066.

121. Jiang XF, et al. Excitation nature of two-photon photoluminescence of gold nanorods and coupled gold nanoparticles studied by two-pulse emission modulation spectroscopy. J Phys Chem Lett. 2013;4:1634–8. https://doi.org/10.1021/jz400582h.

122. Horneber A, et al. Nonlinear optical imaging of single plasmonic nanoparticles with 30 nm resolution. Phys Chem Chem Phys. 2015;17:21288–93. https://doi.org/10.1039/c4cp05342g.
123. Wang N, et al. Ultrafast laser melting of Au nanoparticles: atomistic simulations. J Nanopart Res. 2011;13:4491–509. https://doi.org/10.1007/s11051-011-0402-3.
124. Zeni C, et al. Data-driven simulation and characterisation of gold nanoparticle melting. Nat Commun. 2021;12:6056. https://doi.org/10.1038/s41467-021-26199-7.
125. Wang J, et al. Approach and coalescence of gold nanoparticles driven by surface thermodynamic fluctuations and atomic interaction forces. ACS Nano. 2016;10:2893–902. https://doi.org/10.1021/acsnano.5b08236.
126. Anger P, et al. Enhancement and quenching of single-molecule fluorescence. Phys Rev Lett. 2006;96:113002. https://doi.org/10.1103/PhysRevLett.96.113002.
127. Viste P, et al. Enhancement and quenching regimes in metal-semiconductor hybrid optical nanosources. ACS Nano. 2010;4:759–64. https://doi.org/10.1021/nn901294d.
128. Shahbazyan TV. Theory of plasmon-enhanced metal photoluminescence. Nano Lett. 2013;13:194–8. https://doi.org/10.1021/nl303851z.
129. Shahbazyan TV, et al. Size-dependent surface plasmon dynamics in metal nanoparticles. Phys Rev Lett. 1998;81:3120–3. https://doi.org/10.1103/PhysRevLett.81.3120.
130. Dulkeith E, et al. Plasmon emission in photoexcited gold nanoparticles. Phys Rev B. 2004;70:205424. https://doi.org/10.1103/PhysRevB.70.205424.
131. Fang Y, et al. Plasmon emission quantum yield of single gold nanorods as a function of aspect ratio. ACS Nano. 2012;6:7177–84. https://doi.org/10.1021/nn3022469.
132. Biagioni P, et al. Dependence of the two-photon photoluminescence yield of gold nanostructures on the laser pulse duration. Phys Rev B. 2009;80:045411. https://doi.org/10.1103/PhysRevB.80.045411.
133. Wang QQ, et al. Highly efficient avalanche multiphoton luminescence from coupled Au nanowires in the visible region. Nano Lett. 2007;7:723–8. https://doi.org/10.1021/nl062964f.
134. Ma Z, et al. Origin of the avalanche-like photoluminescence from metallic nanowires. Sci Rep. 2016;6:18857. https://doi.org/10.1038/srep18857.
135. Gong HM, et al. Strong near-infrared avalanche photoluminescence from Ag nanowire arrays. Plasmonics. 2008;3:59–64. https://doi.org/10.1007/s11468-008-9054-2.
136. Song M, et al. Polarization properties of surface plasmon enhanced photoluminescence from a single Ag nanowire. Opt Express. 2012;20:22290–7. https://doi.org/10.1364/OE.20.022290.
137. Wang J, et al. Hot carrier-mediated avalanche multiphoton photoluminescence from coupled Au-Al nanoantennas. J Chem Phys. 2021;154:074701. https://doi.org/10.1063/5.0032611.
138. Hellwarth R, Christensen P. Nonlinear optical microscopic examination of structure in polycrystalline ZnSe. Opt Commun. 1974;12:318–22. https://doi.org/10.1016/0030-4018(74)90024-8.
139. Pavone FS, Campagnola PJ. Second harmonic generation imaging. New York: CRC Press; 2016.
140. Carvalho BR, et al. Nonlinear dark-field imaging of one-dimensional defects in monolayer dichalcogenides. Nano Lett. 2020;20:284–91. https://doi.org/10.1021/acs.nanolett.9b03795.
141. Oka H. Highly-efficient entangled two-photon absorption with the assistance of plasmon nanoantenna. J Phys B: Atomic, Mol Opt Phys. 2015;48:115503. https://doi.org/10.1088/0953-4075/48/11/115503.
142. Smolyaninov A, et al. Plasmonic enhanced two-photon absorption in silicon photodetectors for optical correlators in the near-infrared. Opt Lett. 2016;41:4445–8. https://doi.org/10.1364/OL.41.004445.
143. Kong L, et al. A novel flurophore-cyano-carboxylic-Ag microhybrid: Enhanced two photon absorption for two-photon photothermal therapy of HeLa cancer cells by targeting mitochondria. Biosens Bioelectron. 2018;108:14–9. https://doi.org/10.1016/j.bios.2018.02.028.
144. Li JL, Gu M. Surface plasmonic gold nanorods for enhanced two-photon microscopic imaging and apoptosis induction of cancer cells. Biomaterials. 2010;31:9492–8. https://doi.org/10.1016/j.biomaterials.2010.08.068.
145. Vickers ET, et al. Two-photon photoluminescence and photothermal properties of hollow gold nanospheres for efficient theranostic applications. J Phys Chem C. 2017;122:13304–13. https://doi.org/10.1021/acs.jpcc.7b09055.
146. Kang Z, et al. Passively mode-locking induced by gold nanorods in erbium-doped fiber lasers. Appl Phys Lett. 2013;103:4. https://doi.org/10.1063/1.4816516.
147. Wang X-D, et al. Microfiber-based gold nanorods as saturable absorber for femtosecond pulse generation in a fiber laser. Appl Phys Lett. 2014;105:16. https://doi.org/10.1063/1.4899133.
148. Shu Y, et al. Gold nanorods as saturable absorber for harmonic soliton molecules generation. Front Chem. 2019;7:715. https://doi.org/10.3389/fchem.2019.00715.
149. Atwater HA, Polman A. Plasmonics for improved photovoltaic devices. Nat Mater. 2010;9:205–13. https://doi.org/10.1038/nmat2629.
150. Wang F, Melosh NA. Plasmonic energy collection through hot carrier extraction. Nano Lett. 2011;11:5426–30. https://doi.org/10.1021/nl203196z.
151. Goykhman I, et al. Locally oxidized silicon surface-plasmon Schottky detector for telecom regime. Nano Lett. 2011;11:2219–24. https://doi.org/10.1021/nl200187v.
152. Berini P, et al. Thin Au surface plasmon waveguide Schottky detectors on p-Si. Nanotechnology. 2012;23:444011. https://doi.org/10.1088/0957-4484/23/44/444011.
153. Knight MW, et al. Photodetection with active optical antennas. Science. 2011;332:702–4. https://doi.org/10.1126/science.1203056.
154. Knight MW, et al. Embedding plasmonic nanostructure diodes enhances hot electron emission. Nano Lett. 2013;13:1687–92. https://doi.org/10.1021/nl400196z.
155. Huang X, et al. Gold nanorods: from synthesis and properties to biological and biomedical applications. Adv Mater. 2009;21:4880–910. https://doi.org/10.1002/adma.200802789.
156. Yang X, et al. Gold Nanomaterials at work in biomedicine. Chem Rev. 2015;115:10410–88. https://doi.org/10.1021/acs.chemrev.5b00193.

157. Olesiak-Banska J, et al. Two-photon absorption and photoluminescence of colloidal gold nanoparticles and nano-clusters. Chem Soc Rev. 2019;48:4087–117. https://doi.org/10.1039/c8cs00849c.
158. Zheng J, et al. Gold Nanorods: The most versatile plasmonic nanoparticles. Chem Rev. 2021;121:13342–453. https://doi.org/10.1021/acs.chemrev.1c00422.
159. Durr NJ, et al. Two-photon luminescence imaging of cancer cells using molecularly targeted gold nanorods. Nano Lett. 2007;7:941–5. https://doi.org/10.1021/nl062962v.
160. Chen S, et al. Symmetry-selective third-harmonic generation from plasmonic metacrystals. Phys Rev Lett. 2014;113:033901. https://doi.org/10.1103/PhysRevLett.113.033901.
161. Li G, et al. Continuous control of the nonlinearity phase for harmonic generations. Nat Mater. 2015;14:607–12. https://doi.org/10.1038/nmat4267.
162. Li G, et al. Nonlinear metasurface for simultaneous control of spin and orbital angular momentum in second harmonic generation. Nano Lett. 2017;17:7974–9. https://doi.org/10.1021/acs.nanolett.7b04451.
163. Li Z, et al. Tripling the capacity of optical vortices by nonlinear metasurface. Laser Photonics Rev. 2018;12:1800164. https://doi.org/10.1002/lpor.201800164.
164. Liu L, et al. Backward phase matching for second harmonic generation in negative-index conformal surface plasmonic metamaterials. Adv Sci. 2018;5:1800661. https://doi.org/10.1002/advs.201800661.
165. Forbes A, et al. Structured light. Nat Photonics. 2021;15:253–62. https://doi.org/10.1038/s41566-021-00780-4.
166. Liu L, et al. Plasmon-induced thermal tuning of few-exciton strong coupling in 2D atomic crystals. Optica. 2021;8:11. https://doi.org/10.1364/optica.436140.
167. Sit A, et al. High-dimensional intracity quantum cryptography with structured photons. Optica. 2017;4:9. https://doi.org/10.1364/optica.4.001006.
168. Zhu Z, et al. Compensation-free high-dimensional free-space optical communication using turbulence-resilient vector beams. Nat Commun. 2021;12:1666. https://doi.org/10.1038/s41467-021-21793-1.
169. Weber M, et al. MINSTED nanoscopy enters the Angstrom localization range. Nat Biotechnol. 2023;41:569–76. https://doi.org/10.1038/s41587-022-01519-4.
170. Woerdemann M, et al. Optical assembly of microparticles into highly ordered structures using Ince-Gaussian beams. Appl Phys Lett. 2011;98:11. https://doi.org/10.1063/1.3561770.
171. Yang Y, et al. Optical trapping with structured light: a review. Adv Photonics. 2021;3:034001. https://doi.org/10.1117/1.Ap.3.3.034001.
172. Yeshchenko OA, et al. Temperature dependence of the surface plasmon resonance in gold nanoparticles. Surf Sci. 2013;608:275–81. https://doi.org/10.1016/j.susc.2012.10.019.
173. Judek J, et al. Titanium nitride as a plasmonic material from near-ultraviolet to very-long-wavelength infrared range. Materials (Basel). 2021;14:22. https://doi.org/10.3390/ma14227095.
174. He W, et al. Plasmonic titanium nitride nanoparticles for in vivo photoacoustic tomography imaging and photo-thermal cancer therapy. Biomaterials. 2017;132:37–47. https://doi.org/10.1016/j.biomaterials.2017.04.007.
175. Chang CC, et al. Highly plasmonic titanium nitride by room-temperature sputtering. Sci Rep. 2019;9:15287. https://doi.org/10.1038/s41598-019-51236-3.
176. Luo J, et al. Tailored organic electro-optic materials and their hybrid systems for device applications. Chem Mater. 2010;23:544–53. https://doi.org/10.1021/cm1022344.
177. Melikyan A, et al. High-speed plasmonic phase modulators. Nat Photonics. 2014;8:229–33. https://doi.org/10.1038/nphoton.2014.9.
178. Karst J, et al. Electrically switchable metallic polymer nanoantennas. Science. 2021;374:612–6. https://doi.org/10.1126/science.abj3433.

Publisher's Note